

Higher-Order Total Directional Variation: Imaging Applications ^{*}

Simone Parisotto[†], Jan Lellmann[‡], Simon Masnou[§], and Carola-Bibiane Schönlieb[¶]

Abstract. We introduce a class of higher-order anisotropic total variation regularisers, which are defined for possibly inhomogeneous, smooth elliptic anisotropies, that extends the Total Generalized Variation (TGV) regulariser and its variants. We propose a primal-dual hybrid gradient approach to approximate numerically the associated gradient flow. This choice of regularisers allows to preserve and enhance intrinsic anisotropic features in images. This is illustrated on various examples from different imaging applications: image denoising, wavelet-based image zooming, and reconstruction of surfaces from scattered height measurements.

Key words. Total directional variation, Anisotropy, Denoising, Wavelet-based zooming, Digital Elevation Map

AMS subject classifications. 47A52, 49M30, 49N45, 65J22, 94A08

1. Introduction. In the last decades, total variation (TV) regularisation has been successfully applied to a variety of imaging problems. In particular since [45], TV plays a crucial role for variational image denoising, deblurring, inpainting, segmentation, magnetic resonance image (MRI) reconstruction and many others, see [12]. While the TV regulariser successfully eliminates noise and at the same time preserves characteristic image features like edges, it still has some shortcomings. A major one is the staircasing effect, resulting into blocky-like images [13, 38]. One approach to mitigate this effect is based on higher order total variation regularisers, see e.g. [17, 18, 40, 49, 60], aiming to eliminate the staircasing effect by higher regularity in homogeneous regions of the image while still allowing for discontinuities in the presence of edges. The total generalized variation (TGV_α^q) regulariser has been proposed in [11] to balance the first q derivatives of u with a regularisation parameter vector α . Another modification of the TV regulariser has been the introduction of directional information in the regularisation, allowing to smooth images in an anisotropic fashion favouring preferred directions, e.g. [5, 62, 7, 22, 51, 27, 35, 33, 24, 23]. A recent combination of directional TV and higher-order derivatives is the directional total generalized variation [20] that equips the TGV_α^q regulariser with one constant preferred smoothing direction.

In this paper we extend the directional total generalized variation introduced in [20] and the third-order directional total variation regulariser introduced in [34] to a new class of di-

^{*}Submitted to the editors DATE.

Funding: SP acknowledges UK EPSRC grant EP/L016516/1 for the University of Cambridge, Cambridge Centre for Analysis DTC. CBS acknowledges support from the EPSRC grants Nr. EP/M00483X/1, EP/K009745/1, the EPSRC centre EP/N014588/1, the Leverhulme Trust project 'Breaking the non-convexity barrier', the Alan Turing Institute TU/B/000071, the CHiPS (Horizon 2020 RISE project grant), the Isaac Newton Institute and the Cantab Capital Institute for the Mathematics of Information. SM acknowledges support from the Labex MILYON/ANR-10-LABX-0070 and the ANR-14-CE27-0019 MIRIAM project grant

[†]CCA, University of Cambridge, Wilberforce Road, Cambridge CB3 0WA, UK (sp751@cam.ac.uk)

[‡]MIC, University of Lübeck, Maria-Goeppert-Straße 3, 23562 Lübeck, DE (jan.lellmann@mic.uni-luebeck.de)

[§]Université Claude Bernard Lyon 1, Institut Camille Jordan, Lyon, France (masnou@math.univ-lyon1.fr)

[¶]DAMTP, University of Cambridge, Wilberforce Road, Cambridge CB3 0WA, UK (cbs31@cam.ac.uk)

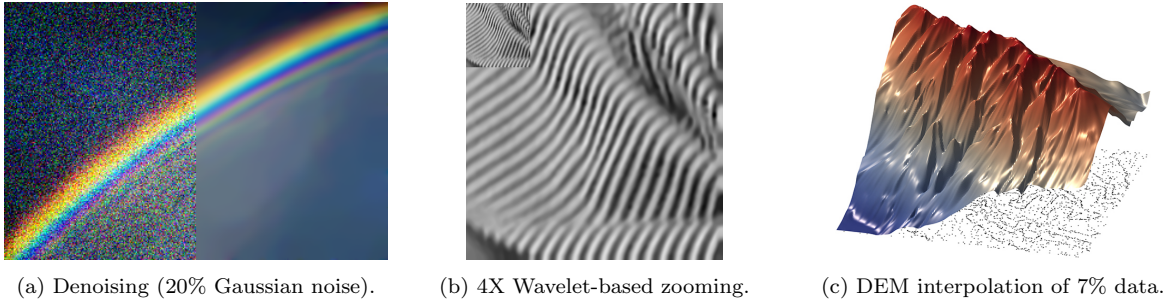


Figure 1.1: Imaging applications for the class of directional regularisers introduced in this paper.

rectional total variation regularisers that can feature a combination of orders of derivatives as well as spatially-varying directional information by means of weighting the derivatives in the TGV_{α}^q regulariser with 2-tensors. We introduce this class of total generalized variation regularisers, discuss its numerical solution by a tailored primal-dual hybrid gradient scheme (which replaces the commercial CVX+Mosek solver used in [34]), and showcase its performance and regularisation properties for a range of imaging problems. For the latter, we show the effect of this generalized class of regularisers in different imaging applications where the introduced anisotropy plays a crucial role: image denoising, wavelet-based zooming and digital elevation map (DEM) interpolation with applications to atomic force microscopy (AFM) data, see Figure 1.1. For the application of our regularisers to video denoising, we refer to [43] and in general to [41]. The theoretical foundation for this general class of directional, higher-order regularisers is presented in our companion work [42].

Let us go into more details. Let $\Omega \subset \mathbb{R}^d$ be a bounded Lipschitz domain for $d \geq 1$ and $u : \Omega \rightarrow \mathbb{R}$ a function, we define the the higher-order directional total variation of u as

$$(1.1) \quad \text{TDV}_{\alpha}^q(u, \mathcal{M}) := \sup_{\Psi} \left\{ \int_{\Omega} u \operatorname{div}_{\mathcal{M}}^q \Psi \, d\mathbf{x} \mid \text{for all } \Psi \in \mathcal{Y}_{\mathcal{M}, \alpha}^q \right\},$$

where we call q the order of the regularisation, \mathcal{M} is a collection of weighting fields, and

$$(1.2) \quad \mathcal{Y}_{\mathcal{M}, \alpha}^q = \left\{ \Psi : \Psi \in C_c^q(\Omega, \mathcal{T}^q(\mathbb{R}^d)), \left\| \operatorname{div}_{\mathcal{M}}^j \Psi \right\|_{\infty} \leq \alpha_j, \forall j = 0, \dots, q-1 \right\},$$

where $\mathcal{T}^q(\mathbb{R}^d)$ is the vector space of q -tensors in \mathbb{R}^d and α is a vector of regularisation parameters. We will provide the rigorous definition for (1.1) in Section 2.2. We comment for now that the regulariser in (1.1) is designed for introducing weighted directional derivatives in the classical definition of TGV_{α}^q . The anisotropy is introduced by a family of weights \mathcal{M} and a thereby suitably weighted divergence $\operatorname{div}_{\mathcal{M}}^q$ of order q , defined in (2.6).

1.1. Related work. In what follows we review the state-of-the-art that is most relevant for the proposed higher-order directional total variation regulariser. We focus in particular on functional regularisers but it is worth mentioning that there is a rich literature on fairly general

anisotropic PDE models, mainly of first and second order, see for instance [46, 53, 57, 31, 9, 14, 3, 61] and the references therein. Our model handles a more limited class of anisotropies but it can do it at any order of derivatives, particularly useful in various applications.

The idea of anisotropic smoothing for imaging has certainly been popularized by the book of Weickert on anisotropic diffusion equations [57] based on the key notion of structure tensor to encode directional information, see also [29, 26, 30]. Weickert's structure tensor for a continuous imaging function $u : \Omega \rightarrow \mathbb{R}$ and non-negative parameters σ, ρ is defined as

$$(1.3) \quad \mathbf{J}_\rho(u) := K_\rho * (\nabla u_\sigma \otimes \nabla u_\sigma),$$

where $u_\sigma = K_\sigma * u$ and K_σ, K_ρ are Gaussian kernels with standard deviations σ, ρ , respectively. For $\nabla u_\sigma \neq 0$ the structure tensor $\mathbf{J}_\rho(u)$ has two orthogonal eigenvectors \mathbf{v}_1 and \mathbf{v}_2 with corresponding non-zero real eigenvalues $\lambda_1(\mathbf{x})$ and $\lambda_2(\mathbf{x})$. Here \mathbf{v}_1 and \mathbf{v}_2 approximately point in the direction ∇u_σ and $\nabla^\perp u_\sigma$. From this, diffusion tensors can be constructed inheriting \mathbf{v}_1 and \mathbf{v}_2 as eigenvectors but whose eigenvalues are expressions of λ_1 and λ_2 so as to increase or reduce smoothing in these directions, compare for instance coherence-enhancing diffusion [58]. The concept of structure tensor is used for variational regularisation in [51] in the framework of a *single orientation estimation* approach. More precisely, the authors consider a regulariser of the type

$$\int_{\Omega} w(\mathbf{x}) \mathbf{J}_\rho(u) \, d\mathbf{x},$$

for a non-negative weight function $w : \Omega \rightarrow \mathbb{R}$ and a continuous imaging function $u : \Omega \rightarrow \mathbb{R}$, for smoothing an image into a dominant single direction. For smoothing a noisy data u^\diamond in two directions, the authors propose to estimate directions \mathbf{v}_1 and \mathbf{v}_2 as in [1] and, in their *double orientation estimation* approach, decompose $u(\mathbf{x}) = u_1(\mathbf{x}) + u_2(\mathbf{x})$ via

$$(1.4) \quad \min_{\substack{u_1, u_2 \\ u_1 + u_2 = u}} \alpha \left(\|\mathbf{v}_1^T \nabla u_1\|_1 + \|\mathbf{v}_2^T \nabla u_2\|_1 \right) + \frac{1}{2} \|u - u^\diamond\|_2^2.$$

An approach based on the analysis of eigenvalues and eigenvectors of the structure tensors can be found in [27] while in [35] the admissible set of test functions are locally adapted to the geometry of \mathbf{u} via the support function regulariser. Furthermore, in [33], the *structure tensor total variation* (STV) focuses on the nuclear norm of the structure tensor (1.3) in order to measure the local image variation:

$$(1.5) \quad \text{STV}_p(u) = \left\| \left(\sqrt{\lambda_1}, \sqrt{\lambda_2} \right) \right\|_p.$$

Also in [24], a regulariser is proposed whose smoothing directions vary according to the image content, leading to the analysis of

$$\mathcal{R}_J(u) = g_\gamma(\mathbf{S} \nabla u), \quad \mathbf{S} = \max \left(\sqrt{\gamma}, \sqrt[4]{\lambda_1 + \lambda_2} \mathbf{\Lambda}^{-0.5} \mathbf{Q}^T \right),$$

where g_γ is the Huber₁ regularisation with parameter $\gamma > 0$ and the structure tensor \mathbf{J}_ρ is eigen-decomposed as $\mathbf{J}_\rho = \mathbf{Q} \mathbf{\Lambda} \mathbf{Q}^T$, with eigenvectors stored in the matrix \mathbf{Q} and the eigenvalues in the diagonal matrix $\mathbf{\Lambda}$.

Let us also mention that early works where the gradient is weighted date back to [7], where the oriented local image structure is extracted from images by the regulariser

$$(1.6) \quad \text{TV}^\alpha(u) = \int_{\Omega} |\mathbf{M}_\alpha \nabla u| \, d\mathbf{x},$$

with \mathbf{M}_α being the orthogonal rotation matrix for an angle $\alpha > 0$.

Further, in [5], a discrete *directional total variation* ($\text{TV}_{a,\theta}$) regulariser for denoising discrete images \mathbf{u} with a single dominant direction (directional images) is introduced via affine transformations of test functions: the circular unit ball generated by the L^2 -norm is transformed into an ellipse $E^{a,\theta}$, with major semiaxis $a > 1$ rotated by θ , penalizing variations for large a along θ :

$$(1.7) \quad \text{TV}_{a,\theta}(\mathbf{u}) = \sum_{i,j} \sup_{\Psi \in E^{a,\theta}} \langle (\nabla \mathbf{u})_{i,j}, \Psi \rangle.$$

In a straightforward generalization of (1.7), inhomogeneous fields θ are allowed, namely $\boldsymbol{\theta} := \theta(\mathbf{x})$. In [62] the authors propose to adapt $\boldsymbol{\theta}$ to the edge directions,

$$(1.8) \quad (\cos \boldsymbol{\theta}, \sin \boldsymbol{\theta}) = \frac{(\nabla u_\sigma)^\perp}{\|\nabla u_\sigma\|_2},$$

so as to associate at each pixel position (i, j) a specific ellipsoid ball $E^{a,\theta_{ij}}$ for the test functions, leading to the discrete *edge adaptive directional total variation* (EADTV) regulariser:

$$(1.9) \quad \text{EADTV}_{\alpha,\boldsymbol{\theta}}(\mathbf{u}) = \sum_{i,j} \sup_{\Psi \in E^{\alpha,\boldsymbol{\theta}_{ij}}} \langle (\nabla \mathbf{u})_{i,j}, \Psi \rangle.$$

In [23], a discrete weighted *directional Total Variation* (dTV) regulariser is introduced as

$$(1.10) \quad \text{dTV}(\mathbf{u}) = \sum_{n=1}^N |\mathcal{P}_{\boldsymbol{\xi}_n} \nabla u_n|, \quad \text{with } \boldsymbol{\xi}_n := \nabla u_n / (K_\sigma * |\nabla u_n|),$$

by projecting onto the complementary part of a vector field $\mathcal{P}_{\boldsymbol{\xi}_n} \mathbf{x} = \mathbf{x} - \langle \boldsymbol{\xi}_n, \mathbf{x} \rangle \boldsymbol{\xi}_n$.

In [20], the continuous *directional total variation* (DTV) and *directional total generalized variation* (DTGV) are analysed for a single homogeneously fixed angle θ and for the minor semi-axis (now denoted with a) of the ellipse $E^{a,\theta}$. There, DTV and DTGV are built upon test functions Ψ in the isotropic ball B_1 , so as to constrain $\tilde{\Psi}$ to the ellipsoid ball, i.e. $\tilde{\Psi} = \mathbf{R}_\theta \boldsymbol{\Lambda}_a \Psi \in E^{a,\theta}$ and where \mathbf{R}_θ and $\boldsymbol{\Lambda}_a$ are rotation and contraction matrices, respectively, similarly to our setting explained later, see Equation (1.14):

$$(1.11) \quad \text{DTV}(u) = \sup_{\tilde{\Psi}} \left\{ \int_{\Omega} u \operatorname{div} \tilde{\Psi} \, d\mathbf{x} \mid \tilde{\Psi} \in C_c^1(\Omega, \mathbb{R}^2) \right\},$$

$$(1.12) \quad \text{DTGV}_\alpha^q(u) = \sup_{\tilde{\Psi}} \left\{ \int_{\Omega} u \operatorname{div}^q \tilde{\Psi} \, d\mathbf{x} \mid \begin{array}{l} \tilde{\Psi} \in C_c^q(\Omega, \operatorname{Sym}^q(\mathbb{R}^2)), \|\operatorname{div}^j \tilde{\Psi}(\mathbf{x})\| \leq \alpha_j, \\ \forall \mathbf{x} \in \Omega \text{ and } \forall j = 0, \dots, q-1 \end{array} \right\}.$$

By comparing (1.12) with (1.1), we immediately note that our proposed setting deals with non-symmetric test functions and directional information inhomogeneously varying in Ω , encoded in a weighted divergence term.

1.2. Our proposal. Our work extends the regularisers in (1.11)-(1.12) for handling spatially varying directions $\boldsymbol{\theta}$ in $\Omega \subset \mathbb{R}^2$ instead of a fixed scalar direction θ . We investigate the directional total variation regulariser of (1.1) and study its performance for a variety of image processing problems by solving

$$(1.13) \quad u^* \in \arg \min_u \sum_{q=1}^Q \text{TDV}_{\alpha_q}^q(u, \mathcal{M}_q) + \frac{\eta}{2} \|\mathcal{S}u - u^\diamond\|_2^2,$$

where $u^\diamond \in L^2(\Omega)$ is a given, imperfect and possibly incomplete imaging data, and $\mathcal{S} : L^2(\Omega) \rightarrow L^2(\Omega)$ a linear operator. We consider the cases for which \mathbf{M}_j in $\mathcal{M}_q = (\mathbf{M}_j)_{j=1}^q$ from (1.1) is

$$\text{either } \mathbf{M}_j = \mathbf{I} \text{ or } \mathbf{M}_j = \boldsymbol{\Lambda}_b(\mathbf{R}_\theta)^\top,$$

with \mathbf{I} the identity, $\boldsymbol{\Lambda}_b$ the contraction and \mathbf{R}_θ the rotation matrices, defined as:

$$(1.14) \quad \boldsymbol{\Lambda}_b = \begin{pmatrix} b_1(\mathbf{x}) & 0 \\ 0 & b_2(\mathbf{x}) \end{pmatrix} \quad \text{and} \quad \mathbf{R}_\theta = \begin{pmatrix} \cos \theta(\mathbf{x}) & -\sin \theta(\mathbf{x}) \\ \sin \theta(\mathbf{x}) & \cos \theta(\mathbf{x}) \end{pmatrix},$$

and with $\mathbf{b} := (b_1(\mathbf{x}), b_2(\mathbf{x}))^\top \in [0, 1]^2$, $\boldsymbol{\theta} := \theta(\mathbf{x}) \in [0, 2\pi)$. Occasionally, we will use the vector field $\mathbf{v} = (\cos \boldsymbol{\theta}, \sin \boldsymbol{\theta})^\top$ and its orthogonal $\mathbf{v}_\perp = (-\sin \boldsymbol{\theta}, \cos \boldsymbol{\theta})^\top$. Thus, we interpret the core operation of the dual version of the regulariser in (1.1), $\mathbf{M}_1 \nabla \otimes u$, as weighted directional derivatives of u along \mathbf{v} and \mathbf{v}_\perp since

$$(1.15) \quad \mathbf{M}_1 \nabla \otimes u = \boldsymbol{\Lambda}_b(\mathbf{R}_\theta)^\top \nabla \otimes u = \begin{pmatrix} b_1 \nabla_{\mathbf{v}} u \\ b_2 \nabla_{\mathbf{v}_\perp} u \end{pmatrix}.$$

We will in particular focus on the case $\mathbf{b} = (1, \beta(\mathbf{x}))$ for $\beta(\mathbf{x}) \in [0, 1]$ being either inhomogeneous or constant in Ω , see Remark 1.1 for the geometrical interpretation when different choices are made for the constant.

Remark 1.1. In Figure 1.2 we simulate the two dimensional behaviour of (1.15) for different choices of b_2 . More precisely, for a continuous imaging function $u : \Omega \rightarrow \mathbb{R}$ we represent a possible situation at the position $\mathbf{x} \in \Omega$ of the vectors $\mathbf{p} = (p_1, p_2) = \nabla u$ and $\mathbf{v} = (v_1, v_2)$, depicted with red and blue arrows, respectively. We also represent the components $\mathbf{r} = (r_1, r_2) = (p_1 v_1, p_2 v_2)$ of $\nabla_{\mathbf{v}} u = r_1 + r_2 = p_1 v_1 + p_2 v_2$ by a green arrow. The vectors and the corresponding arrows are the same in all Figure 1.2a to Figure 1.2f. Moreover, the test functions $\boldsymbol{\Psi} = (\Psi^1, \Psi^2)$ lie on the black circle due to the constraint $\|\boldsymbol{\Psi}\|_2 \leq 1$. Note that in the 2D domain we have

$$\mathbf{M}_1 \nabla u \cdot \boldsymbol{\Psi} = \nabla u \cdot \mathbf{M}_1^\top \boldsymbol{\Psi},$$

which allows to change the metric space of the test functions into an elliptic ball in magenta. Being fixed $b_1 = 1$, each figure corresponds to a particular choice of $b_2 = \beta$ between 0 and 1. Finally, the magenta arrow corresponds to the direction of $\boldsymbol{\Psi}$ which realizes the supremum of the regulariser TDV_α^1 in Equation (1.1). We observe in Figure 1.2f the limit case $\mathbf{b} = (1, 0)$ where $\text{TDV}_\alpha^1(u, \mathcal{M})$ penalizes the rate of change of u only along \mathbf{v} without orthogonal \mathbf{v}_\perp contribution. In all the other circumstances, \mathbf{v}_\perp acts as quality estimation of \mathbf{v} , leading to a full isotropic approach in the case $\mathbf{b} = (1, 1)$ of Figure 1.2a, since the magenta arrow is bended in the direction of the gradient ∇u rather than the direction of $\nabla_{\mathbf{v}} u$.

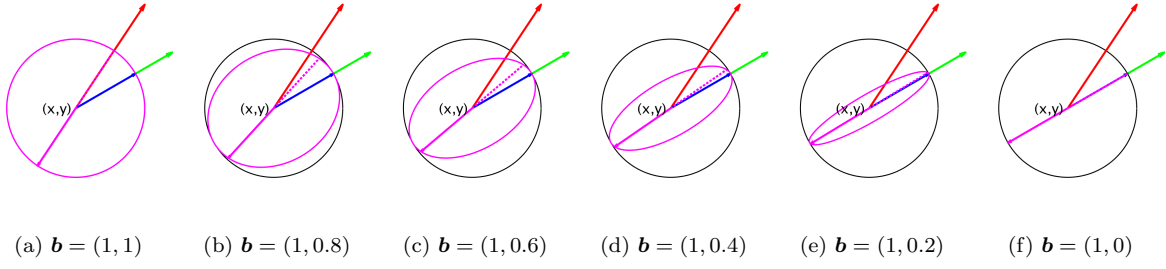


Figure 1.2: Different choices for $\mathbf{b} = (1, \beta)$ in $\text{TDV}_\alpha^1(u, \mathcal{M})$, with $\mathcal{M} = \mathbf{\Lambda}_\mathbf{b}(\mathbf{R}_\theta)^\top$ and θ fixed.

1.3. Contribution of the paper. In what follows we will derive:

- a rigorous definition of the total directional regulariser (1.1);
- a characterisation of (1.1) that turns (1.13) into a form that is amenable for numerical solution. For this we propose a primal-dual algorithm and present certain instances for different combinations of orders $q = 1, \dots, Q$, up to $Q = 3$ in (1.1);
- a number of numerical experiments with this new regulariser for image denoising, image zooming and interpolation of two-dimensional surfaces from a sparse number of given height values.

1.4. Organization of the paper. In Section 2 we discuss the higher-order total directional variation regularisers with anisotropy. The numerical details of the discretisation are introduced in Section 3, with the primal-dual algorithm and the numerical optimisation described in Section 4. Imaging applications to denoising, wavelet-based zooming and surface interpolation, e.g. in atomic force microscopy imaging, are discussed in Section 5 and Section 6.

2. Higher-order total directional variation. In this section we introduce the rigorous definition of (1.1). To do so, we first introduce the terminology of tensors and their mathematical manipulation.

2.1. Tensors. Following [11], let $\mathcal{T}^\ell(\mathbb{R}^d)$ be the vector space of ℓ -tensors defined as

$$\mathcal{T}^\ell(\mathbb{R}^d) := \left\{ \boldsymbol{\xi} : \underbrace{\mathbb{R}^d \times \dots \times \mathbb{R}^d}_{\ell\text{-times}} \rightarrow \mathbb{R}, \text{ such that } \boldsymbol{\xi} \text{ is } \ell\text{-linear} \right\}.$$

On $\mathcal{T}^\ell(\mathbb{R}^d)$, we have the following operations:

- let \otimes be the tensor product for $\boldsymbol{\xi}_1 \in \mathcal{T}^{\ell_1}(\mathbb{R}^d)$, $\boldsymbol{\xi}_2 \in \mathcal{T}^{\ell_2}(\mathbb{R}^d)$, with $\boldsymbol{\xi}_1 \otimes \boldsymbol{\xi}_2 \in \mathcal{T}^{\ell_1 + \ell_2}(\mathbb{R}^d)$:

$$(\boldsymbol{\xi}_1 \otimes \boldsymbol{\xi}_2)(\mathbf{a}_1, \dots, \mathbf{a}_{\ell_1 + \ell_2}) = \boldsymbol{\xi}_1(\mathbf{a}_1, \dots, \mathbf{a}_{\ell_1}) \boldsymbol{\xi}_2(\mathbf{a}_{\ell_1 + 1}, \dots, \mathbf{a}_{\ell_1 + \ell_2});$$

- let $\text{trace}(\boldsymbol{\xi}) \in \mathcal{T}^{\ell-2}(\mathbb{R}^d)$ be the trace of $\boldsymbol{\xi} \in \mathcal{T}^\ell(\mathbb{R}^d)$, with $\ell \geq 2$, defined by

$$\text{trace}(\boldsymbol{\xi})(\mathbf{a}_1, \dots, \mathbf{a}_{\ell-2}) = \sum_{i=1}^d \boldsymbol{\xi}(\mathbf{e}_i, \mathbf{a}_1, \dots, \mathbf{a}_{\ell-2}, \mathbf{e}_i),$$

where \mathbf{e}_i is the i -th standard basis vector;

- let $(\cdot)^\sim$ be such that if $\xi \in \mathcal{T}^\ell(\mathbb{R}^d)$, then $\xi^\sim(\mathbf{a}_1, \dots, \mathbf{a}_\ell) = \xi(\mathbf{a}_\ell, \mathbf{a}_1, \dots, \mathbf{a}_{\ell-1})$;
- let $\bar{(\cdot)}$ be such that if $\xi \in \mathcal{T}^\ell(\mathbb{R}^d)$, then $\bar{\xi}(\mathbf{a}_1, \dots, \mathbf{a}_\ell) = \xi(\mathbf{a}_\ell, \dots, \mathbf{a}_1)$;
- let $\xi, \eta \in \mathcal{T}^\ell(\mathbb{R}^d)$. The space $\mathcal{T}^\ell(\mathbb{R}^d)$ is equipped with the scalar product defined as

$$\xi \cdot \eta = \sum_{p \in \{1, \dots, d\}^\ell} \xi_{p_1, \dots, p_\ell} \eta_{p_1, \dots, p_\ell}.$$

We now introduce the derivative operator for tensors and its weighted version.

Definition 2.1. Let $\nabla = (\partial_1, \dots, \partial_d)^\top$ be the derivative operator and $\xi \in \mathcal{T}^\ell(\mathbb{R}^d)$. The derivative of ξ is defined as $(\nabla \otimes \xi) \in \mathcal{T}^{\ell+1}(\mathbb{R}^d)$ via the following:

$$\nabla \otimes \xi := (\partial_j \xi_{i_1, \dots, i_\ell})_{j, i_1, \dots, i_\ell}.$$

Let $\eta \in \mathcal{T}^2(\mathbb{R}^d)$. The derivative operator weighted by η is defined as $\eta \nabla \in \mathcal{T}^1(\mathbb{R}^d)$ and the derivative of $\xi \in \mathcal{T}^\ell(\mathbb{R}^d)$ weighted by η is defined as $(\eta \nabla \otimes \xi) \in \mathcal{T}^{\ell+1}(\mathbb{R}^d)$ via the following:

$$(2.1) \quad \eta \nabla \otimes \xi := \left(\sum_{k=1}^d \eta_{j,k} \partial_k \xi_{i_1, \dots, i_\ell} \right)_{j, i_1, \dots, i_\ell}.$$

Remark 2.2. For notational purposes, the sum in (2.1) will be shortened using Einstein notation over the repeated subscript, meaning that each element of the tensor $\eta \nabla \otimes \xi$ is written as $\eta_{j,k} \partial_k \xi_{i_1, \dots, i_\ell}$.

In what follows, we will also denote the space of q -times uniformly continuously differentiable $\mathcal{T}^\ell(\mathbb{R}^d)$ -valued tensors as $C^q(\bar{\Omega}, \mathcal{T}^\ell(\mathbb{R}^d))$ which is a Banach space with the norm

$$\|u\|_{\infty, q} = \max_{\ell=0, \dots, q} \sup_{x \in \Omega} \left| \nabla^\ell \otimes u(x) \right|,$$

where $(\nabla^q \otimes u) : \Omega \rightarrow \mathcal{T}^{q+\ell}(\mathbb{R}^d)$, and we will consider also the space $C_c^q(\Omega, \mathcal{T}^\ell(\mathbb{R}^d))$ of $\mathcal{T}^\ell(\mathbb{R}^d)$ -valued tensors which are q -times continuously differentiable with compact support in Ω .

2.2. Definition of total directional variation. For making sense of the distributional formulation of higher-order directional variation in (1.1) we need an integration by parts formula for the weighted derivative of tensors in Definition 2.1. Namely we consider

$$\int_{\Omega} (\mathbf{M} \nabla \otimes \mathbf{A}) \cdot \Psi \, d\mathbf{x},$$

with $\Omega \subset \mathbb{R}^d$ being a bounded Lipschitz domain, $\mathbf{M} \in C^1(\Omega, \mathcal{T}^2(\mathbb{R}^d))$, $\mathbf{A} \in C^1(\Omega, \mathcal{T}^\ell(\mathbb{R}^d))$ and $\Psi \in C_c^1(\Omega, \mathcal{T}^{\ell+1}(\mathbb{R}^d))$. We report in this section the main results from the second part of our companion work [42], where detailed proofs can be found. First, we give an integration by parts formula where only \mathbf{M} switches:

Lemma 2.3. Let Ω , \mathbf{M} , \mathbf{A} and Ψ as above. Then:

$$(2.2) \quad \int_{\Omega} (\mathbf{M} \nabla \otimes \mathbf{A}) \cdot \Psi \, d\mathbf{x} = \int_{\Omega} (\nabla \otimes \mathbf{A}) \cdot \text{trace}(\mathbf{M} \otimes \Psi^\sim) \, d\mathbf{x}, \quad \text{for all } \mathbf{M}, \mathbf{A}, \Psi.$$

Then a general adjoint property follows:

Lemma 2.4. *Let Ω , \mathbf{M} , \mathbf{A} and Ψ as above. Then:*

$$(2.3) \quad \int_{\Omega} (\mathbf{M} \nabla \otimes \mathbf{A}) \cdot \Psi \, d\mathbf{x} = - \int_{\Omega} \mathbf{A} \cdot \operatorname{div}_{\mathbf{M}} \Psi \, d\mathbf{x}, \quad \text{for all } \mathbf{M}, \mathbf{A}, \Psi,$$

where $\operatorname{div}_{\mathbf{M}} \Psi := \operatorname{trace}(\nabla \otimes [\operatorname{trace}(\mathbf{M} \otimes \Psi^{\sim})]^{\sim})$.

We can now define the *total directional variation* of order q with weights $\alpha \in \mathbb{R}_+^q$.

Definition 2.5. *Let $\Omega \subset \mathbb{R}^d$, $u \in L^1(\Omega, \mathbb{R})$, $q \in \mathbb{N}$, $\mathcal{M} := (\mathbf{M}_j)_{j=1}^q$ be a collection of fields in $C^\infty(\Omega, \mathcal{T}^2(\mathbb{R}^d))$ and $\alpha := (\alpha_0, \dots, \alpha_{q-1})$ be a positive weight vector. Then, the total directional variation of order q , associated to \mathcal{M} and α , is defined as:*

$$(2.4) \quad \operatorname{TDV}_{\alpha}^q(u, \mathcal{M}) := \sup_{\Psi} \left\{ \int_{\Omega} u \operatorname{div}_{\mathcal{M}}^q \Psi \, d\mathbf{x} \mid \text{for all } \Psi \in \mathcal{Y}_{\mathcal{M}, \alpha}^q \right\},$$

where

$$(2.5) \quad \mathcal{Y}_{\mathcal{M}, \alpha}^q = \left\{ \Psi : \Psi \in C_c^q(\Omega, \mathcal{T}^q(\mathbb{R}^d)), \left\| \operatorname{div}_{\mathcal{M}}^j \Psi \right\|_{\infty} \leq \alpha_j, \forall j = 0, \dots, q-1 \right\},$$

and the weighted divergence of order q is defined recursively, from [Lemma 2.4](#), as:

$$(2.6) \quad \begin{aligned} \operatorname{div}_{\mathcal{M}}^0 \Psi &:= \Psi, & \text{if } j = 0, \\ \operatorname{div}_{\mathcal{M}}^1 \Psi &:= \operatorname{div}_{\mathbf{M}_q} \Psi, & \text{if } j = 1, \\ &\vdots & \vdots \\ \operatorname{div}_{\mathcal{M}}^q(\Psi) &:= \operatorname{div}_{\mathbf{M}_{q-j+1}} \left(\operatorname{div}_{\mathcal{M}}^{j-1} \Psi \right) & \text{if } j = 2, \dots, q. \end{aligned}$$

Remark 2.6. For $\mathcal{M} = (\mathbf{I})_{j=1}^q$, then $\operatorname{TDV}_{\alpha}^q(u, \mathcal{M}) \equiv \neg\operatorname{symTGV}_{\alpha}^q(u)$, see [\[42\]](#) and [\[11, Remark 3.10\]](#).

2.3. Directional matrices for applications. In what follows, we introduce a particular parametrisation of directional matrices for fields \mathcal{M} in [\(2.4\)](#). For standard imaging applications, we will usually deal with grey-scale images $u : \Omega \rightarrow \mathbb{R}$, $\Omega \subset \mathbb{R}^2$, i.e. $d = 2$.

Definition 2.7 (Directional matrices). *Let $(\mathbf{b}^j)_{j=1}^q$, $\mathbf{b}^j : \Omega \rightarrow [0, 1]^2$, be a collection of so-called contraction weights (being each element of modulus ≤ 1), $(\boldsymbol{\theta}^j)_{j=1}^q$, $\boldsymbol{\theta}^j : \Omega \rightarrow [0, 2\pi)$, be a collection of angles, and $\mathbf{\Lambda}_{\mathbf{b}}^j$ and $\mathbf{R}_{\boldsymbol{\theta}}^j$ the associated contraction and rotation matrices defined, respectively, as*

$$\mathbf{\Lambda}_{\mathbf{b}}^j := \begin{pmatrix} \mathbf{b}_1^j & 0 \\ 0 & \mathbf{b}_2^j \end{pmatrix}, \quad \mathbf{R}_{\boldsymbol{\theta}}^j := \begin{pmatrix} \cos \boldsymbol{\theta}^j & -\sin \boldsymbol{\theta}^j \\ \sin \boldsymbol{\theta}^j & \cos \boldsymbol{\theta}^j \end{pmatrix} \in \operatorname{SO}(2).$$

Then we define $\mathcal{M} := (\mathbf{M}_j)_{j=1}^q$ to be a collection of contraction-rotation matrices (in Einstein notation) as

$$\mathbf{M}_j := \mathbf{\Lambda}_{\mathbf{b}}^j (\mathbf{R}_{\boldsymbol{\theta}}^j)^{\top} = \left(\lambda_{pk}^j r_{\ell k}^j \right)_{p, \ell},$$

where $\lambda_{pk}^j, r_{\ell k}^j$ are the element-wise entries of the matrices $\mathbf{\Lambda}_{\mathbf{b}}^j, \mathbf{R}_{\boldsymbol{\theta}}^j$, respectively.

Definition 2.8 (Weighted derivatives of order 1). Let $\nabla = (\partial_1, \partial_2)^\top$ be the derivative operator. The gradient of a differentiable imaging function u is given by $\nabla u := \nabla \otimes u = (\partial_1 u, \partial_2 u)^\top$ and the weighted derivative operator of order 1 associated to the directional matrix \mathbf{M}_1 from Definition 2.7 is

$$\mathbf{M}_1 \nabla u := (\mathbf{M}_1 \nabla \otimes u)_p = (\lambda_{pk}^1 r_{\ell k}^1 \partial_\ell u)_p.$$

Remark 2.9. If $\mathbf{M}_1 = \mathbf{I}$ (i.e. $b_1^1 \equiv b_2^1 \equiv 1$ and $\theta^q \equiv 0$ for all $\mathbf{x} \in \Omega$), then $\mathbf{M}_1 \nabla u \equiv \nabla u$.

Remark 2.10. Given θ_1 , let $\mathbf{v}^1 = (\cos \theta^1, \sin \theta^1)$ and $\mathbf{v}_\perp^1 = (-\sin \theta^1, \cos \theta^1)$. Then

$$\mathbf{M}_1 \nabla \otimes u := \begin{pmatrix} \mathbf{b}_1^1 \nabla_{\mathbf{v}^1} u \\ \mathbf{b}_2^1 \nabla_{\mathbf{v}_\perp^1} u \end{pmatrix},$$

where $\nabla_{\mathbf{z}} u$ represents the directional derivative along a vector field \mathbf{z} , defined as

$$\nabla_{\mathbf{z}} u(\mathbf{x}) = \nabla u(\mathbf{x}) \cdot \mathbf{z} = \sum_{i=1}^2 \partial_i u z_i.$$

Definition 2.11 (Weighted derivatives of order q). We define the derivative of order q of u using Definition 2.8 recursively as

$$\nabla^q u := (\nabla \otimes \nabla^{q-1} u)_{p_q, \dots, p_1} = (\partial_{p_q} \dots \partial_{p_1} u)_{p_q, \dots, p_1}.$$

We define the weighted derivative of order q of u with respect to \mathcal{M} recursively as

$$\nabla_{\mathcal{M}}^0 u := u,$$

$$\nabla_{\mathcal{M}}^1 u := (\mathbf{M}_1 \nabla \otimes u)_{p_1} = (\lambda_{p_1 k}^1 r_{\ell k}^1 \partial_\ell u)_{p_1},$$

⋮

$$\nabla_{\mathcal{M}}^q u := ((\mathbf{M}_q \nabla) \otimes (\mathbf{M}_{q-1} \nabla^{q-1} u))_{p_q, \dots, p_1} = \left(\lambda_{p_q k_q}^q r_{\ell_q k_q}^q \partial_{\ell_q} (\mathbf{M}_{q-1} \nabla^{q-1} \otimes u) \right)_{p_q, p_{q-1}, \dots, p_1}.$$

2.4. Examples. We present some examples of the total directional variation of order q for $q = 1, 2, 3$, $\alpha = (\alpha_j)_{j=0}^{q-1}$ and a collection of directional matrices $\mathcal{M} = (\mathbf{M}_j)_{j=1}^q$:

- order $q = 1$ and $\mathcal{M} = (\mathbf{M}_1)$:

$$\text{TDV}_\alpha^1(u, \mathcal{M}) := \sup_{\Psi} \left\{ \int_{\Omega} u \operatorname{div}_{\mathbf{M}_1} \Psi \, d\mathbf{x} \mid \text{for all } \Psi \in \mathcal{Y}_{\mathcal{M}, \alpha}^1 \right\},$$

$$\mathcal{Y}_{\mathcal{M}, \alpha}^1 = \{ \Psi : \Psi \in C_c^\infty(\Omega, \mathbb{R}^2) \text{ s.t. } \|\Psi\|_\infty \leq \alpha_0 \};$$

- order $q = 2$ and $\mathcal{M} = (\mathbf{M}_1, \mathbf{M}_2)$:

$$\text{TDV}_\alpha^2(u, \mathcal{M}) := \sup_{\Psi} \left\{ \int_{\Omega} u \operatorname{div}_{\mathbf{M}_1} (\operatorname{div}_{\mathbf{M}_2} \Psi) \, d\mathbf{x} \mid \text{for all } \Psi \in \mathcal{Y}_{\mathcal{M}, \alpha}^2 \right\},$$

$$\mathcal{Y}_{\mathcal{M}, \alpha}^2 = \{ \Psi : \Psi \in C_c^\infty(\Omega, \mathbb{R}^{2 \times 2}) \text{ s.t. } \|\Psi\|_\infty \leq \alpha_0, \|\operatorname{div}_{\mathbf{M}_2} \Psi\|_\infty \leq \alpha_1 \};$$

- order $q = 3$ and $\mathcal{M} = (\mathbf{M}_1, \mathbf{M}_2, \mathbf{M}_3)$:

$$\text{TDV}_\alpha^3(u, \mathcal{M}) := \sup_{\Psi} \left\{ \int_{\Omega} u \operatorname{div}_{\mathbf{M}_1} (\operatorname{div}_{\mathbf{M}_2} (\operatorname{div}_{\mathbf{M}_3} \Psi)) \, d\mathbf{x} \mid \text{for all } \Psi \in \mathcal{Y}_{\mathcal{M}, \alpha}^3 \right\},$$

$$\mathcal{Y}_{\mathcal{M}, \alpha}^3 = \left\{ \Psi : \Psi \in C_c^\infty(\Omega, \mathbb{R}^{2 \times 2 \times 2}) \text{ s.t. } \begin{pmatrix} \|\Psi\|_\infty \leq \alpha_0 \\ \|\operatorname{div}_{\mathbf{M}_3} \Psi\|_\infty \leq \alpha_1 \\ \|\operatorname{div}_{\mathbf{M}_2} (\operatorname{div}_{\mathbf{M}_3} \Psi)\|_\infty \leq \alpha_2 \end{pmatrix} \right\}.$$

3. Numerical discretisation. The rest of the paper focuses on the discretised formulation of (1.13), and its numerical solutions and performances on a number of image processing variational examples. We start by discretising the $\text{TDV}_\alpha^q - L^2$ problem in (1.13).

3.1. Staggered grids. The discretisation of the $\text{TDV}_\alpha^q - L^2$ in (1.13) is based on finite-difference schemes for derivatives on staggered regular Cartesian grids of width $h > 0$:

- the *grid of pixels* Ω^h , of axes x_1 and x_2 for a 2-dimensional domain and size $M \times N$, is defined as

$$\Omega^h = \{(kh, lh) \mid (1, 1) \leq (k, l) \leq (M, N)\};$$

- the *grid of cell centres* Γ^h , of size $(M-1) \times (N-1)$ and used to perform the weighted derivative operation (i.e. for introducing the anisotropy, see the grid associated to the blue squares in Figure 3.1), is defined as:

$$\Gamma^h = \left\{ (\tilde{k}h, \tilde{l}h) \mid (\tilde{k}, \tilde{l}) = \left(k + \frac{1}{2}, l + \frac{1}{2}\right), (1, 1) \leq (k, l) < (M, N) \right\};$$

- the collection of *grids* $\left(X_{\boldsymbol{\iota}}^{j,h}\right)_{j=1}^q$ associated to the differential operators involved, where $\boldsymbol{\iota} = (\iota_1, \dots, \iota_j)$ is a multi-index variable and $\iota_s \in \{1, 2\}$ for each $s = 1, \dots, j$ indicates the partial derivative involved (1 for ∂_{x_1} and 2 for ∂_{x_2}). Every $X_{\boldsymbol{\iota}}^{j,h}$ is a sub-collection of 2^j grids, each one of size $M \times N$ and denoted by $X_{(\iota_1, \dots, \iota_j)}^{j,h}$, each one associated to a fixed choice for the derivative operator $\left(\partial_{x_{\iota_j}} \cdots \partial_{x_{\iota_1}}\right)$ considered:

$$X_{(i_1, \dots, i_j)}^{j,h} = \left\{ (mh, nh) \mid (m, n) = \left(k + \frac{|I_1|_{\#}}{2}, l + \frac{|I_2|_{\#}}{2}\right), (1, 1) \leq (k, l) \leq (M, N) \right\},$$

where $|I_1|_{\#}$ and $|I_2|_{\#}$ are the cardinality of the sets I_1 and I_2 containing as many elements as the number of derivatives along the axes x_1 and x_2 , respectively. A visual representation of such grids is given in Figure 3.1. For example:

- with a bit of abuse of notation, if $j = 0$ then $X_{(-)}^{0,h}$ coincides with Ω^h ;
- $X_{(1)}^{1,h}, X_{(2)}^{1,h}$ result in Ω^h shifted by $h/2$ along x_1 and x_2 axes, respectively;
- if $q = 3$ and $\boldsymbol{\iota} = (2, 1, 1)$, then we are referring to the grid associated to one out of the eight possible combinations for the third order derivative ∇^3 , namely $\partial_{x_2} \partial_{x_1} \partial_{x_1}$, which is located on the grid identified by our notation $X_{(1,1,2)}^{3,h}$.

3.2. Discretised objects. Let the order of derivatives $q > 0$ be fixed. By means of the superscript h , we define the finite-dimensional approximation of the following quantities, where $|\Omega^h|$, $|\Gamma^h|$ and $|X_{(\ell_1, \dots, \ell_j)}^{j,h}|$ are the number of grid points in Ω^h , Γ^h and $X_{(\ell_1, \dots, \ell_j)}^{j,h}$, respectively:

- $\mathbf{u}^h \in \mathbb{R}^{|\Omega^h|}$ is the discretisation of the function u ;
- $\mathbf{u}^{\diamond, h}$ is the discretisation of the observed imaging data u^\diamond ;
- $\mathbf{v}^h = (\mathbf{v}_1^h, \mathbf{v}_2^h) \in \mathbb{R}^{|\Gamma^h| \times |\Gamma^h|}$ is a discrete vector field;
- $\mathbf{b}^h = (\mathbf{b}_1^h, \mathbf{b}_2^h) \in \mathbb{R}^{|\Gamma^h| \times |\Gamma^h|}$ are discrete contraction weights for $\Lambda_{\mathbf{b}}$;
- $\mathbf{M}_j^h \in \mathbb{R}^{|\Gamma^h| \times |\Gamma^h| \times |\Gamma^h| \times |\Gamma^h|}$ discretises the weights $\mathbf{M}_j \in \mathcal{T}^2(\mathbb{R}^2)$, for each $j = 1, \dots, q$;
- $\mathcal{M}^h = (\mathbf{M}_j^h)_{j=1}^q$ discretises the collection of weights $\mathcal{M} = (\mathbf{M}_j)_{j=1}^q$;
- $\Psi^h = (\Psi_1^h, \dots, \Psi_{2q}^h) \in \mathbb{R}^{|\Gamma^h| \times \dots \times |\Gamma^h|}$ discretises the test functions $\Psi \in \mathcal{T}^q(\mathbb{R}^2)$;
- $\mathbf{z}^h = (\mathbf{z}_j^h)_{j=0}^{q-1}$ discretises the primal variables \mathbf{z} , with $\mathbf{z}_0^h = \mathbf{u}^h \in \mathbb{R}^{|\Omega^h|}$, $\mathbf{z}_0^{\diamond, h} = \mathbf{u}^{\diamond, h}$ and each $\mathbf{z}_j^h \in \mathbb{R}^{|\mathbb{X}_{(1, \dots, 1)}^{j,h}| \times \dots \times |\mathbb{X}_{(2, \dots, 2)}^{j,h}|}$, for $j = 1, \dots, q-1$;
- $\mathbf{w}^h = (\mathbf{w}_j^h)_{j=1}^q$ discretises the dual variables \mathbf{w} , with $\mathbf{w}_j^h \in \mathbb{R}^{|\mathbb{X}_{(1, \dots, 1)}^{j,h}| \times \dots \times |\mathbb{X}_{(2, \dots, 2)}^{j,h}|}$ for $j = 1, \dots, q$.

3.3. Isotropic differential operators. Here we discuss the discretization of the adjoint unweighted operators ∇ and div . For $\mathbf{u}^h \in \mathbb{R}^{|\Omega^h|}$, the *discrete gradient* operator is defined as

$$\begin{aligned} \nabla^h : \mathbb{R}^{|\Omega^h|} &\rightarrow \mathbb{R}^{|\mathbb{X}_{(1)}^{1,h}| \times |\mathbb{X}_{(2)}^{1,h}|} \\ \mathbf{u}^h &\mapsto (\partial_1^h \mathbf{u}^h, \partial_2^h \mathbf{u}^h), \end{aligned}$$

where we use the *central second-order finite difference scheme* on the grids $\mathbb{X}_{(1)}^{1,h}$, $\mathbb{X}_{(2)}^{1,h}$:

$$(\partial_1^h \mathbf{u}^h)_{k+\frac{1}{2}, l} = \begin{cases} \frac{u_{k+1, l}^h - u_{k, l}^h}{2 \left(\frac{h}{2}\right)} & \text{if } k < M, \\ 0 & \text{if } k = M, \end{cases} \quad \text{and} \quad (\partial_2^h \mathbf{u}^h)_{k, l+\frac{1}{2}} = \begin{cases} \frac{u_{k, l+1}^h - u_{k, l}^h}{2 \left(\frac{h}{2}\right)} & \text{if } l < N, \\ 0 & \text{if } l = N. \end{cases}$$

Let $\mathbf{p}^h = (\mathbf{p}_1^h, \mathbf{p}_2^h) \in \mathbb{R}^{|\mathbb{X}_{(1)}^{1,h}| \times |\mathbb{X}_{(2)}^{1,h}|}$ and let the *discrete divergence* operator

$$\begin{aligned} \text{div}^h : \mathbb{R}^{|\mathbb{X}_{(1)}^{1,h}| \times |\mathbb{X}_{(2)}^{1,h}|} &\rightarrow \mathbb{R}^{|\Omega^h|} \\ \mathbf{p}^h &\mapsto \nabla^h \cdot \mathbf{p}^h, \end{aligned}$$

be defined for each pixel (k, l) via the *central second-order difference scheme* on Ω^h :

$$(\text{div}^h \mathbf{p}^h)_{k, l} = \begin{cases} \frac{(\mathbf{p}_1^h)_{k+\frac{1}{2}, l}}{2 \left(\frac{h}{2}\right)} & \text{if } k = 1, \\ \frac{(\mathbf{p}_1^h)_{k+\frac{1}{2}, l} - (\mathbf{p}_1^h)_{k-\frac{1}{2}, l}}{2 \left(\frac{h}{2}\right)} & \text{if } k \in (1, M), \\ -\frac{(\mathbf{p}_1^h)_{k-\frac{1}{2}, l}}{2 \left(\frac{h}{2}\right)} & \text{if } k = M, \end{cases} + \begin{cases} \frac{(\mathbf{p}_2^h)_{k, l+\frac{1}{2}}}{2 \left(\frac{h}{2}\right)} & \text{if } l = 1, \\ \frac{(\mathbf{p}_2^h)_{k, l+\frac{1}{2}} - (\mathbf{p}_2^h)_{k, l-\frac{1}{2}}}{2 \left(\frac{h}{2}\right)} & \text{if } l \in (1, N), \\ -\frac{(\mathbf{p}_2^h)_{k, l-\frac{1}{2}}}{2 \left(\frac{h}{2}\right)} & \text{if } l = N. \end{cases}$$

Thus, the isotropic *discrete gradient* and *discrete divergence* are designed to fulfil the discrete adjointness property, for every $\mathbf{u}^h \in \mathbb{R}^{|\Omega^h|}$ and $\mathbf{p}^h \in \mathbb{R}^{|\mathbb{X}_{(1)}^{1,h}| \times |\mathbb{X}_{(2)}^{1,h}|}$:

$$(3.1) \quad \langle \nabla^h \mathbf{u}^h, \mathbf{p}^h \rangle_{\Gamma^h} = \langle \mathbf{u}^h, \operatorname{div}^h \mathbf{p}^h \rangle_{\Omega^h},$$

where $\langle \cdot, \cdot \rangle_{\Gamma^h} : \mathbb{R}^{|\mathbb{X}_{(1)}^{1,h}| \times |\mathbb{X}_{(2)}^{1,h}|} \times \mathbb{R}^{|\mathbb{X}_{(1)}^{1,h}| \times |\mathbb{X}_{(2)}^{1,h}|} \rightarrow \mathbb{R}$ and $\langle \cdot, \cdot \rangle_{\Omega^h} : \mathbb{R}^{|\Omega^h|} \times \mathbb{R}^{|\Omega^h|} \rightarrow \mathbb{R}$.

For higher-order derivatives of order q we denote the isotropic *discrete gradient* and *discrete divergence* operator by $\nabla^{q,h}$ and $\operatorname{div}^{q,h}$ and write

$$\begin{aligned} \nabla^{q,h} : \mathbb{R}^{|\Omega^h|} &\rightarrow \mathbb{R}^{|\mathbb{X}_{(1,\dots,1)}^{q,h}| \times \dots \times |\mathbb{X}_{(\iota_1,\dots,\iota_q)}^{q,h}| \times \dots \times |\mathbb{X}_{(2,\dots,2)}^{q,h}|} \\ \mathbf{u}^h &\mapsto \left(\partial_1^h (\partial_1^h (\dots (\partial_1^h \mathbf{u}^h))), \dots, \partial_{\iota_q}^h (\partial_{\iota_{q-1}}^h \dots (\partial_{\iota_1}^h \mathbf{u}^h)), \dots, \partial_2^h (\partial_2^h (\dots \partial_2^h \mathbf{u}^h)) \right), \end{aligned}$$

and

$$\begin{aligned} \operatorname{div}^{q,h} : \mathbb{R}^{|\mathbb{X}_{(1,\dots,1)}^{q,h}| \times \dots \times |\mathbb{X}_{(2,\dots,2)}^{q,h}|} &\rightarrow \mathbb{R}^{|\Omega^h|} \\ \mathbf{p}^h &\mapsto \nabla^{q,h} \cdot \mathbf{p}^h. \end{aligned}$$

The adjointness property is fulfilled for every $\mathbf{u}^h \in \mathbb{R}^{|\Omega^h|}$ and $\mathbf{p}^h \in \mathbb{R}^{|\mathbb{X}_{(1,\dots,1)}^{q,h}| \times \dots \times |\mathbb{X}_{(2,\dots,2)}^{q,h}|}$:

$$(3.2) \quad \langle \nabla^{q,h} \mathbf{u}^h, \mathbf{p}^h \rangle_{\Gamma^h} = \langle \mathbf{u}^h, \operatorname{div}^{q,h} \mathbf{p}^h \rangle_{\Omega^h},$$

with $\langle \cdot, \cdot \rangle_{\Gamma^h} : \mathbb{R}^{|\mathbb{X}_{(1,\dots,1)}^{q,h}| \times \dots \times |\mathbb{X}_{(2,\dots,2)}^{q,h}|} \times \mathbb{R}^{|\mathbb{X}_{(1,\dots,1)}^{q,h}| \times \dots \times |\mathbb{X}_{(2,\dots,2)}^{q,h}|} \rightarrow \mathbb{R}$ and $\langle \cdot, \cdot \rangle_{\Omega^h} : \mathbb{R}^{|\Omega^h|} \times \mathbb{R}^{|\Omega^h|} \rightarrow \mathbb{R}$.

3.4. Transfer operators. The offset in the location between \mathbf{z}_0^h , $\nabla^{1,h} \mathbf{z}_0^h$, \dots , $\nabla^{q,h} \mathbf{z}_0^h$ and the fields \mathcal{M}^h associated to \mathbf{v}^h requires the introduction of *transfer operators*, a concept from multigrid methods [52], so as to make the quantities computable in the same location. In what follows, we will provide some insights for the general case.

Let $\mathcal{W} := (\mathcal{W}^j)_{j=1}^q$ be a family of transfer operators $\mathcal{W}^j = (\mathbf{W}_\iota^j)$, with $\mathbf{W}_\iota^j : \mathbb{R}^{|\mathbb{X}_\iota^{j,h}|} \rightarrow \mathbb{R}^{|\Gamma^h|}$ and ι a multi-index variable, with entries in $\{1, 2\}$ similarly as for the staggered grids $\mathbb{X}_\iota^{j,h}$. The idea is that \mathcal{W}^j interpolates the data from the grids of j -th order derivatives $\mathbb{X}_\iota^{j,h}$ to the grid of cell centres Γ^h , e.g. \mathbf{W}_ι^j is the operator made by partition of unit weights. Since it is an averaging matrix, its adjoint operation is denoted by $(\mathcal{W}^j)^\top$, where the extension from Γ^h to the boundary of $\mathbb{X}_\iota^{j,h}$ is made possible by mirroring the data as appropriate.

Example 3.1. For $\mathbf{z}_0^h \in \mathbb{R}^{|\Omega^h|}$ and q fixed, the derivatives of \mathbf{z}_0^h (up to order q) are

$$\begin{aligned} \mathbf{w}_1^h &:= \nabla^{1,h} \mathbf{z}_0^h = (\partial_1^h \mathbf{z}_0^h, \partial_2^h \mathbf{z}_0^h) \in \mathbb{R}^{|\mathbb{X}_{(1)}^{1,h}| \times |\mathbb{X}_{(2)}^{1,h}|}, \\ \mathbf{w}_2^h &:= \nabla^{2,h} \mathbf{z}_0^h = (\partial_1^h \partial_1^h \mathbf{z}_0^h, \partial_1^h \partial_2^h \mathbf{z}_0^h, \partial_2^h \partial_1^h \mathbf{z}_0^h, \partial_2^h \partial_2^h \mathbf{z}_0^h) \in \mathbb{R}^{|\mathbb{X}_{(1,1)}^{2,h}| \times |\mathbb{X}_{(2,1)}^{2,h}| \times |\mathbb{X}_{(1,2)}^{2,h}| \times |\mathbb{X}_{(2,2)}^{2,h}|}, \\ &\vdots \\ \mathbf{w}_q^h &:= \nabla^{q,h} \mathbf{z}_0^h = (\partial_1^h \dots \partial_1^h \mathbf{z}_0^h, \dots, \partial_2^h \dots \partial_2^h \mathbf{z}_0^h) \in \mathbb{R}^{|\mathbb{X}_{(1,\dots,1)}^{q,h}| \times \dots \times |\mathbb{X}_{(2,\dots,2)}^{q,h}|}, \end{aligned}$$

the transfer operators $\mathcal{W} = (\mathcal{W}^j)_{j=1}^q$ are

$$\mathcal{W}^j := \begin{cases} \mathbf{W}_{(1,\dots,1)}^j : \mathbb{R}^{|X_{(1,\dots,1)}^{j,h}|} \rightarrow \mathbb{R}^{|\Gamma^h|}, \\ \vdots \\ \mathbf{W}_{(\ell_1,\dots,\ell_j)}^j : \mathbb{R}^{|X_{(\ell_1,\dots,\ell_j)}^{j,h}|} \rightarrow \mathbb{R}^{|\Gamma^h|}, \\ \vdots \\ \mathbf{W}_{(2,\dots,2)}^j : \mathbb{R}^{|X_{(2,\dots,2)}^{j,h}|} \rightarrow \mathbb{R}^{|\Gamma^h|}, \end{cases}$$

and each $\mathbf{W}_{(\ell_1,\dots,\ell_j)}^j$ is the interpolation matrix that interpolates the values of $(\partial_{\ell_j} \dots \partial_{\ell_1} \mathbf{z}_0^h) \in \mathbb{R}^{|X_{(\ell_1,\dots,\ell_j)}^{j,h}|}$ to $\mathbb{R}^{|\Gamma^h|}$ by an arithmetic mean. For example, for the first order derivatives we have

$$\mathcal{W}^1 \nabla^{1,h} \otimes \mathbf{u}^h = (\mathbf{W}_{(1)}^1 \partial_1^h \mathbf{u}^h, \mathbf{W}_{(2)}^1 \partial_2^h \mathbf{u}^h) \in \mathbb{R}^{|\Gamma^h| \times |\Gamma^h|},$$

where, for $k = 1, \dots, M-1$ and $l = 1, \dots, N-1$,

$$\begin{aligned} (\mathbf{W}_{(1)}^1 \partial_1^h \mathbf{u}^h)_{k+\frac{1}{2},l+\frac{1}{2}} &= \frac{(\partial_1^h \mathbf{u}^h)_{k+\frac{1}{2},l} + (\partial_1^h \mathbf{u}^h)_{k+\frac{1}{2},l+1}}{2}, \\ (\mathbf{W}_{(2)}^1 \partial_2^h \mathbf{u}^h)_{k+\frac{1}{2},l+\frac{1}{2}} &= \frac{(\partial_2^h \mathbf{u}^h)_{k,l+\frac{1}{2}} + (\partial_2^h \mathbf{u}^h)_{k+1,l+\frac{1}{2}}}{2}. \end{aligned}$$

As a further example for the second order derivative case and $\mathbf{M}_1^h = \mathbf{I}$ (which implies no averaging on the first derivatives for our construction), we have

$$\mathcal{W}^2 \nabla^{1,h} \otimes \nabla^{1,h} \otimes \mathbf{u}^h = (\mathbf{W}_{(1,1)}^2 \partial_1^h \partial_1^h \mathbf{u}^h, \mathbf{W}_{(2,1)}^2 \partial_1^h \partial_2^h \mathbf{u}^h, \mathbf{W}_{(1,2)}^2 \partial_2^h \partial_1^h \mathbf{u}^h, \mathbf{W}_{(2,2)}^2 \partial_2^h \partial_2^h \mathbf{u}^h),$$

where $\mathcal{W}^2 \nabla^{1,h} \otimes \nabla^{1,h} \otimes \mathbf{u}^h \in \mathbb{R}^{|\Gamma^h| \times |\Gamma^h| \times |\Gamma^h| \times |\Gamma^h|}$ and, for $k = 1, \dots, M-1$ and $l = 1, \dots, N-1$,

$$\begin{aligned} (\mathbf{W}_{(1,1)}^2 \partial_1^h \partial_1^h \mathbf{u}^h)_{k+\frac{1}{2},l+\frac{1}{2}} &= \frac{(\partial_1^h \partial_1^h \mathbf{u}^h)_{k,l} + (\partial_1^h \partial_1^h \mathbf{u}^h)_{k-1,l+1}}{2}, \\ (\mathbf{W}_{(2,1)}^2 \partial_1^h \partial_2^h \mathbf{u}^h)_{k+\frac{1}{2},l+\frac{1}{2}} &= (\partial_1^h \partial_2^h \mathbf{u}^h)_{k,l}, \\ (\mathbf{W}_{(1,2)}^2 \partial_2^h \partial_1^h \mathbf{u}^h)_{k+\frac{1}{2},l+\frac{1}{2}} &= (\partial_2^h \partial_1^h \mathbf{u}^h)_{k,l}, \\ (\mathbf{W}_{(2,2)}^2 \partial_2^h \partial_2^h \mathbf{u}^h)_{k+\frac{1}{2},l+\frac{1}{2}} &= \frac{(\partial_2^h \partial_2^h \mathbf{u}^h)_{k,l} + (\partial_2^h \partial_2^h \mathbf{u}^h)_{k+1,l-1}}{2}, \end{aligned}$$

with $(\partial_1^h \partial_1^h \mathbf{u}^h)_{0,l} = (\partial_1^h \partial_1^h \mathbf{u}^h)_{1,l}$ and $(\partial_2^h \partial_2^h \mathbf{u}^h)_{k,0} = (\partial_2^h \partial_2^h \mathbf{u}^h)_{k,1}$.

Remark 3.2. The choice of the staggered grid increases the accuracy of the solution and allows to compute the inner products between gradients and the vector fields onto a unique regular Cartesian grid of reference, avoiding offsets. Moreover, the transfer operators \mathcal{W} reduce the bandwidth of higher order finite difference matrices, improving the quality of the result and reducing the smoothing due to large stencils.

Remark 3.3. Note that when $\mathbf{M}_j^h = \mathbf{I}$ and $\alpha_j = +\infty$ for every $j < q$, as in the applications described in Section 6 of this paper, the use of transfer operators is needed only for the outer derivative, i.e. the one associated to the weighting field \mathbf{M}_q^h .

We report in Figure 3.1 the positions of $\nabla^{q,h}$, up to order $q = 3$, in order to illustrate how transfer operators \mathcal{W} work in interpolating the data on Γ^h .

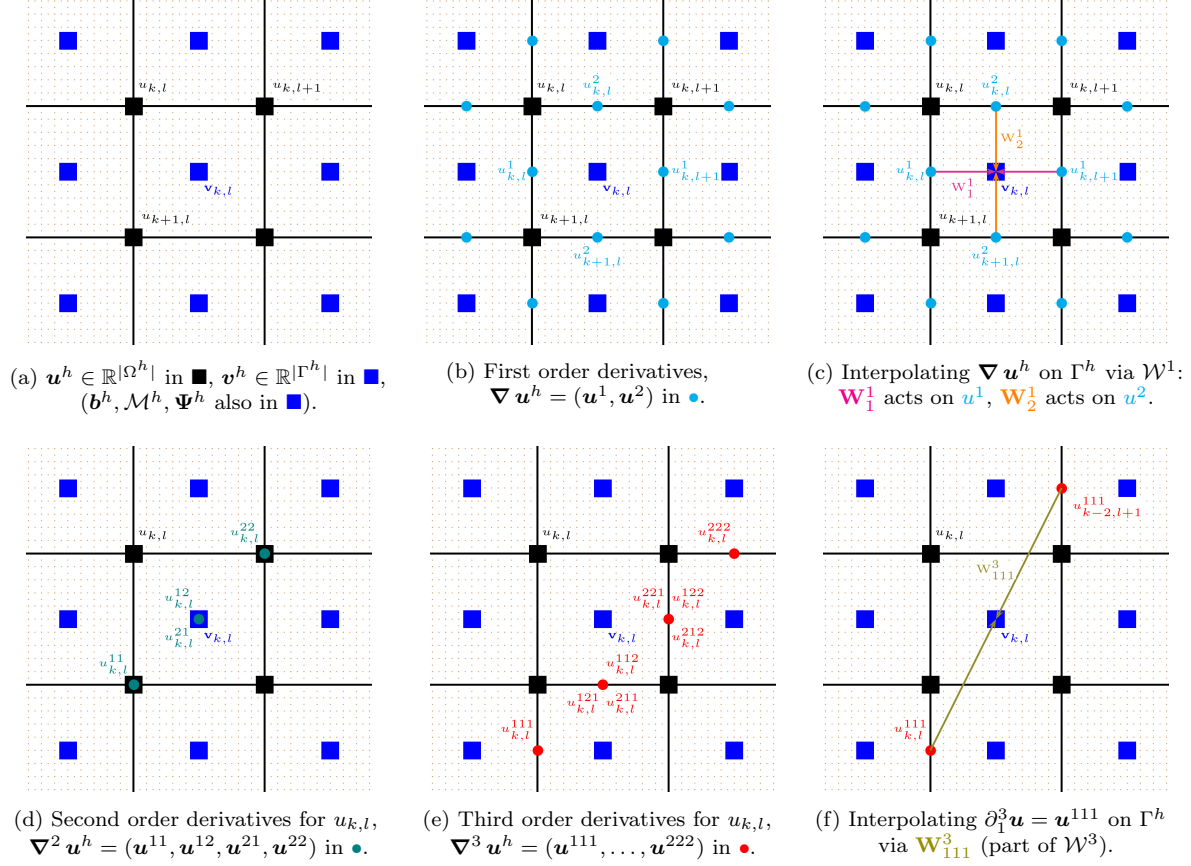


Figure 3.1: Staggered grids with higher-order derivatives defined via iterative central finite differences of half stepsize, visualisation of variables and examples of transfer operators. Derivatives of \mathbf{u}^h , denoted by superscripts, are located on coloured bullets. The transfer operators \mathcal{W} interpolate values from coloured bullets to blue squares and vice-versa.

3.5. Anisotropic differential operators. By construction, $\mathbf{M}_1^h \in \mathbb{R}^{|\Gamma^h| \times |\Gamma^h| \times |\Gamma^h| \times |\Gamma^h|}$ and $\nabla^{1,h} \mathbf{u}^h \in \mathbb{R}^{|\mathbf{X}_{(1)}^{1,h}| \times |\mathbf{X}_{(2)}^{1,h}|}$ so the grids $\mathbf{X}_{(1)}^{1,h}, \mathbf{X}_{(2)}^{1,h}$ have an $(h/2)$ -offset with respect to Γ^h . In this case, locations of $\nabla^{1,h} \mathbf{u}^h$ and \mathbf{M}_1^h are matched via the transfer operators $\mathcal{W}^1 = (\mathbf{W}_{(1)}^1, \mathbf{W}_{(2)}^1)$.

From Remark 2.10, $\mathbf{M}_1 \nabla \otimes u$ can be discretised in the correct grid position by the operator

$$\mathbf{M}_1^h \mathcal{W}^1 \nabla^{1,h} : \mathbb{R}^{|\Omega^h|} \rightarrow \mathbb{R}^{|\Gamma^h| \times |\Gamma^h|},$$

and the discretisation reads as

$$\mathbf{M}_1^h \mathcal{W}^1 \nabla^{1,h} \otimes \mathbf{u}^h = \begin{pmatrix} \mathbf{b}_1^h \mathcal{W}^1 \nabla^{1,h} \mathbf{u}^h \cdot \mathbf{v}^h \\ \mathbf{b}_2^h \mathcal{W}^1 \nabla^{1,h} \mathbf{u}^h \cdot \mathbf{v}_\perp^h \end{pmatrix} = \begin{pmatrix} \mathbf{b}_1^h \left(\mathbf{W}_{(1)}^1 \partial_1^h \mathbf{u}^h \mathbf{v}_1^h + \mathbf{W}_{(2)}^1 \partial_2^h \mathbf{u}^h \mathbf{v}_2^h \right) \\ \mathbf{b}_2^h \left(\mathbf{W}_{(2)}^1 \partial_2^h \mathbf{u}^h \mathbf{v}_1^h - \mathbf{W}_{(1)}^1 \partial_1^h \mathbf{u}^h \mathbf{v}_2^h \right) \end{pmatrix}.$$

Therefore, the discrete weighted divergence $\operatorname{div}_{\mathbf{M}_1^h, \mathcal{W}^1}^h \mathbf{p}^h : \mathbb{R}^{|\Gamma^h| \times |\Gamma^h|} \rightarrow \mathbb{R}^{|\Omega^h|}$ is

$$(3.3) \quad \operatorname{div}_{\mathbf{M}_1^h, \mathcal{W}^1}^h \mathbf{p}^h = \nabla^{1,h} \cdot \begin{pmatrix} (\mathbf{W}_{(1)}^1)^\top (\mathbf{b}_1^h \mathbf{p}_1^h \mathbf{v}_1^h - \mathbf{b}_2^h \mathbf{p}_2^h \mathbf{v}_2^h) \\ (\mathbf{W}_{(2)}^1)^\top (\mathbf{b}_1^h \mathbf{p}_1^h \mathbf{v}_2^h + \mathbf{b}_2^h \mathbf{p}_2^h \mathbf{v}_1^h) \end{pmatrix}.$$

This leads to the discrete adjointness property, for every $\mathbf{u}^h \in \mathbb{R}^{|\Omega^h|}$, $\mathbf{p}^h \in \mathbb{R}^{|\Gamma^h| \times |\Gamma^h|}$:

$$(3.4) \quad \langle \mathbf{M}_1^h \mathcal{W}^1 \nabla^{1,h} \mathbf{u}^h, \mathbf{p}^h \rangle_{\Gamma^h} = \langle \mathbf{u}^h, \operatorname{div}_{\mathbf{M}_1^h, \mathcal{W}^1}^h \mathbf{p}^h \rangle_{\Omega^h},$$

where $\langle \cdot, \cdot \rangle_{\Gamma^h} : \mathbb{R}^{|\Gamma^h| \times |\Gamma^h|} \times \mathbb{R}^{|\Gamma^h| \times |\Gamma^h|} \rightarrow \mathbb{R}$ and $\langle \cdot, \cdot \rangle_{\Omega^h} : \mathbb{R}^{|\Omega^h|} \times \mathbb{R}^{|\Omega^h|} \rightarrow \mathbb{R}$.

When considering higher order derivatives for a generic order q , the adjoint formula (3.4) is slightly more complicated due to the recursive definition of the weighted gradient and the location of the nested multiplication. Indeed by Definition 2.11 we have for a fixed q $\nabla_{\mathcal{M}}^q u := \mathbf{M}_q \nabla \otimes \cdots \otimes \mathbf{M}_1 \nabla \otimes u$, whose finite-dimensional approximation is formally written as $\nabla_{\mathcal{M}^h, \mathcal{W}}^{q,h} \mathbf{u}^h : \mathbb{R}^{|\Omega^h|} \rightarrow \mathbb{R}^{|\Gamma^h| \times \cdots \times |\Gamma^h|}$ via the recursion rule

$$(3.5) \quad \nabla_{\mathcal{M}^h, \mathcal{W}}^{j,h} \mathbf{u}^h := \begin{cases} \mathbf{u}^h & \text{if } j = 0, \\ (\mathcal{W}^j)^\top \mathbf{M}_j^h \mathcal{W}^j \nabla^{1,h} \otimes \nabla_{\mathcal{M}^h, \mathcal{W}}^{j-1,h} \mathbf{u}^h & \text{if } j = 1, \dots, q-1, \\ \mathbf{M}_q^h \mathcal{W}^q \nabla^{1,h} \otimes \nabla_{\mathcal{M}^h, \mathcal{W}}^{j-1,h} \mathbf{u}^h & \text{if } j = q. \end{cases}$$

The finite-dimensional approximation of the adjoint $\operatorname{div}_{\mathcal{M}}^q$ is denoted with $\operatorname{div}_{\mathcal{M}^h, \mathcal{W}}^{q,h} : \mathbb{R}^{|\Gamma^h| \times \cdots \times |\Gamma^h|} \rightarrow \mathbb{R}^{|\Omega^h|}$ and defined via the recursion rule

$$(3.6) \quad \operatorname{div}_{\mathcal{M}^h, \mathcal{W}}^{j,h} \Psi^h := \begin{cases} \Psi^h & \text{if } j = 0, \\ \mathcal{W}^{q-j} \nabla^{1,h} \cdot (\mathcal{W}^{q-j+1})^\top (\mathbf{M}_{q-j+1}^h)^\top \operatorname{div}_{\mathcal{M}^h, \mathcal{W}}^{j-1,h} \Psi^h & \text{if } j = 1, \dots, q-1, \\ \nabla^{1,h} \cdot (\mathcal{W}^1)^\top (\mathbf{M}_1^h)^\top \operatorname{div}_{\mathcal{M}^h, \mathcal{W}}^{q-1,h} \Psi^h & \text{if } j = q. \end{cases}$$

Remark 3.4. Note that in (3.5) for $j = q$ we omitted the inverse transfer operator $(\mathcal{W}^q)^\top$ so as to force the highest derivative $\nabla_{\mathcal{M}^h, \mathcal{W}}^{q,h} \mathbf{u}^h$ to be located in $\mathbb{R}^{|\Gamma^h| \times \cdots \times |\Gamma^h|}$ and match with the position of Ψ^h . For the same reason, in (3.6) we omitted the transfer operator for $j = q$ so as to match the quantity with \mathbf{u}^h in the grid Ω . This operation is performed in view of the adjointness property stated below in (3.7).

For every $\mathbf{u}^h \in \mathbb{R}^{|\Omega^h|}$, $\mathbf{p}^h \in \mathbb{R}^{|\Gamma^h| \times \cdots \times |\Gamma^h|}$, the discrete adjointness property holds:

$$(3.7) \quad \langle \nabla_{\mathcal{M}^h, \mathcal{W}}^{q,h} \mathbf{u}^h, \mathbf{p}^h \rangle_{\Gamma^h} = \langle \mathbf{u}^h, \operatorname{div}_{\mathcal{M}^h, \mathcal{W}}^{q,h} \mathbf{p}^h \rangle_{\Omega^h},$$

where $\langle \cdot, \cdot \rangle_{\Gamma^h} : \mathbb{R}^{|\Omega^h| \times \cdots \times |\Gamma^h|} \times \mathbb{R}^{|\Gamma^h| \times \cdots \times |\Gamma^h|} \rightarrow \mathbb{R}$ and $\langle \cdot, \cdot \rangle_{\Omega^h} : \mathbb{R}^{|\Omega^h|} \times \mathbb{R}^{|\Omega^h|} \rightarrow \mathbb{R}$.

4. Numerical optimisation. In what follows, we solve in the first instance the single line version of (1.13), namely for a fixed $q > 0$, a fixed $\alpha = (\alpha_j)_{j=0}^{q-1}$, a fixed collection of weighting matrices $\mathcal{M} = (\mathbf{M}_j)_{j=1}^q$ and \mathcal{S} the operator associated to the problem to solve, we aim to tackle the problem

$$(4.1) \quad \min_{\mathbf{u} \in \mathbb{R}^{|\Omega^h|}} \text{TDV}_{\alpha}^q(\mathbf{u}, \mathcal{M}) + \frac{\eta}{2} \|\mathcal{S}\mathbf{u}_0 - \mathbf{u}_0^{\diamond, h}\|_2^2,$$

by means of a primal-dual hybrid gradient method [15, 16] and following [11, Equation 4.4]. With all discrete objects in place, we have

$$\min_{\mathbf{z}_0^h \in \mathbb{R}^{|\Omega^h|}} \text{TDV}_{\alpha}^{q,h}(\mathbf{z}_0^h, \mathcal{M}^h) + \frac{\eta}{2} \|\mathcal{S}\mathbf{z}_0^h - \mathbf{z}_0^{\diamond, h}\|_2^2,$$

where $\mathbf{z}_0^{\diamond, h} = \mathbf{u}^{\diamond, h} \in \mathbb{R}^{|\Omega^h|}$, $\text{div}_{\mathcal{M}^h, \mathcal{W}}^{q,h}$ is the discretized weighted divergence w.r.t. the weights \mathcal{M}^h and the transfer operators \mathcal{W} , $\text{TDV}_{\alpha}^{q,h}$ is the discrete version of TDV_{α}^q defined as

$$\text{TDV}_{\alpha}^{q,h}(\mathbf{z}_0^h, \mathcal{M}^h) = \sup_{\Psi^h \in \mathcal{Y}_{\mathcal{M}^h, \alpha}^{q,h}} \langle \mathbf{z}_0^h, \text{div}_{\mathcal{M}^h, \mathcal{W}}^{q,h} \Psi^h \rangle,$$

and $\mathcal{Y}_{\mathcal{M}^h, \alpha}^{q,h}$ is the discretization of $\mathcal{Y}_{\mathcal{M}, \alpha}^q$ in (2.5), defined as

$$(4.2) \quad \mathcal{Y}_{\mathcal{M}^h, \alpha}^{q,h} = \left\{ \Psi^h \in \mathbb{R}^{2q|\Gamma^h|} \mid \left\| \text{div}_{\mathcal{M}^h, \mathcal{W}}^{j,h} \Psi^h \right\|_{\infty} \leq \alpha_j, \text{ for all } j = 0, \dots, q-1 \right\}.$$

4.1. Discrete characterisation of TDV. For a fixed $q > 0$, the regulariser $\text{TDV}_{\alpha}^{q,h}$ can be characterised as follows. From the discrete version of TGV_{α}^q in [50, Section 4.1] and following the characterization of TGV_{α}^q in [11, Remark 3.8 and Remark 3.10], we can write the equivalent discrete definition of $\text{TDV}_{\alpha}^q(\mathbf{u}, \mathcal{M})$ for $\mathbf{u}^h \in \mathbb{R}^{|\Omega^h|}$ and $\mathcal{M}^h = (\mathbf{M}_j^h)_{j=1}^q$ as

$$(4.3) \quad \text{TDV}_{\alpha}^{q,h}(\mathbf{u}^h, \mathcal{M}^h) = \inf_{\substack{\mathbf{z}_j^h \in \mathbb{R}^{|\mathbf{X}_j^h|} \\ j=0, \dots, q \\ \mathbf{z}_0 = \mathbf{u}^h, \mathbf{z}_q = \mathbf{0}}} \sum_{j=1}^q \alpha_{q-j} \|\mathcal{K}_{j,j}^h \mathbf{z}_{j-1}^h - \mathbf{z}_j^h\|_1,$$

where

$$(4.4) \quad \mathcal{K}_{j,j}^h = \begin{cases} (\mathcal{W}^j)^{\text{T}} \mathbf{M}_j^h \mathcal{W}^j \nabla^h & \text{if } j = 1, \dots, q-1, \\ \mathbf{M}_q^h \mathcal{W}^q \nabla^h & \text{if } j = q. \end{cases}$$

Indeed, in the following let $j = 1, \dots, q$, $\mathbf{w}_{q-j+1}^h \in \mathbb{R}^{|\mathbf{X}_j^{q-j+1}|}$ and $\mathbf{z}_{q-j}^h \in \mathbb{R}^{|\mathbf{X}_j^{q-j,h}|}$. We call

$$\text{DV}_{\alpha}^{j,h}(\mathbf{w}_{q-j+1}^h, \mathcal{M}^h) = \sup_{\Psi^h \in \mathcal{Y}_{\mathcal{M}^h, \alpha}^{q,h}} -\langle (\mathcal{W}^{q-j+1})^{\text{T}} \mathbf{M}_{q-j+1}^h \mathcal{W}^{q-j+1} \mathbf{w}_{q-j+1}^h, \text{div}_{\mathcal{M}^h, \mathcal{W}}^{j-1} \Psi^h \rangle,$$

where $\operatorname{div}_{\mathcal{M}^h, \mathcal{W}}^{j-1}$ as in (3.6) and $\mathcal{Y}_{\mathcal{M}^h, \alpha}^{q,h}$ as in (4.2). Note that the sup is finite by definition of $\mathcal{Y}_{\mathcal{M}^h, \alpha}^{q,h}$. Thus $\operatorname{TDV}_{\alpha}^{q,h}(\mathbf{u}^h, \mathcal{M}^h) = \operatorname{DV}_{\alpha}^{q,h}(\nabla^h \mathbf{u}^h, \mathcal{M}^h)$ and we define

$$K_{\ell}^h = \left\{ \Psi^h : \Psi^h \in \mathcal{Y}_{\mathcal{M}^h, \alpha}^{j,h}, \left\| \operatorname{div}_{\mathcal{M}^h, \mathcal{W}}^{\ell,h} \Psi^h \right\|_{\infty} \leq \alpha_{\ell} \right\} \quad \text{for every } \ell = 0, \dots, q-1.$$

With $\mathbf{s}_{q,j}^h = \mathbf{M}_q^h \mathcal{W}^q \nabla^h \otimes \dots \otimes (\mathcal{W}^{q-j+2})^T \mathbf{M}_{q-j+2}^h \mathcal{W}^{q-j+2} \nabla^h$ and $(j-1)$ -times integration by parts, the functional becomes

$$\operatorname{DV}_{\alpha}^{j,h}(\mathbf{w}_{q-j+1}^h, \mathcal{M}^h) = \left(\sum_{\ell=0}^{j-1} \delta_{K_{\ell}^h} \right)^* \left((-1)^j \mathbf{s}_{q,j}^h \otimes (\mathcal{W}^{q-j+1})^T \mathbf{M}_{q-j+1}^h \mathcal{W}^{q-j+1} \mathbf{w}_{q-j+1}^h \right),$$

where $\delta_{K_{\ell}^h}$ is the characteristic function with values either 0 or $+\infty$, and where the adjoint $*$ is the same as in [11, Remark 3.9]. By Fenchel duality for the operator $\operatorname{div}_{\mathcal{M}^h, \mathcal{W}}^{j-1,h}$ we have:

$$\begin{aligned} \operatorname{DV}_{\alpha}^{j,h}(\nabla^h \mathbf{z}_{q-j}^h, \mathcal{M}^h) &= \sup_{\Psi^h \in \mathbb{R}^{2^q |\Gamma^h|}} \left(\begin{aligned} & - \langle (\mathcal{W}^{q-j+1})^T \mathbf{M}_{q-j+1}^h \mathcal{W}^{q-j+1} \nabla^h \mathbf{z}_{q-j}^h, \operatorname{div}_{\mathcal{M}^h, \mathcal{W}}^{j-1,h} \Psi^h \rangle \\ & - \delta_{K_{j-1}^h}(\Psi^h) - \sum_{\ell=0}^{j-2} \delta_{K_{\ell}^h}(\Psi^h) \end{aligned} \right) \\ &= \sup_{\Psi^h \in \mathbb{R}^{2^q |\Gamma^h|}} \left(\begin{aligned} & - \sum_{\ell=0}^{j-2} \delta_{K_{\ell}^h}(\Psi^h) - \delta_{\{\|\cdot\| \leq \alpha_{j-1}\}}(\operatorname{div}_{\mathcal{M}^h, \mathcal{W}}^{j-1,h} \Psi^h) \\ & - \langle (\mathcal{W}^{q-j+1})^T \mathbf{M}_{q-j+1}^h \mathcal{W}^{q-j+1} \nabla^h \mathbf{z}_{q-j}^h, \operatorname{div}_{\mathcal{M}^h, \mathcal{W}}^{j-1,h} \Psi^h \rangle \end{aligned} \right) \\ &= \inf_{\mathbf{z}_{q-j+1}^h \in \mathbb{R}^{|\mathbb{X}_{\ell}^{q-j+1,h}|}} \left(\begin{aligned} & \alpha_{j-1} \left\| (\mathcal{W}^{q-j+1})^T \mathbf{M}_{q-j+1}^h \mathcal{W}^{q-j+1} \nabla^h \mathbf{z}_{q-j}^h - \mathbf{z}_{q-j+1}^h \right\|_1 \\ & + \left(\sum_{\ell=0}^{j-2} \delta_{K_{\ell}^h} \right)^* \left((-1)^{j-1} \mathbf{s}_{q,j+1}^h \mathbf{z}_{q-j+1}^h \right) \end{aligned} \right) \\ &= \inf_{\mathbf{z}_{q-j+1}^h \in \mathbb{R}^{|\mathbb{X}_{\ell}^{q-j+1,h}|}} \left(\begin{aligned} & \alpha_{j-1} \left\| (\mathcal{W}^{q-j+1})^T \mathbf{M}_{q-j+1}^h \mathcal{W}^{q-j+1} \nabla^h \mathbf{z}_{q-j}^h - \mathbf{z}_{q-j+1}^h \right\|_1 \\ & + \operatorname{DV}_{\alpha}^{j-1,h}(\nabla^h \mathbf{z}_{q-j+1}^h, \mathcal{M}^h) \end{aligned} \right). \end{aligned}$$

Iterating the procedure for $j = q, \dots, 2$ and by the identity

$$\operatorname{DV}_{\alpha}^{1,h}(\nabla^h \mathbf{z}_{q-1}^h) = \alpha_0 \left\| \mathbf{M}_q^h \mathcal{W}^q \nabla^h \mathbf{z}_{q-1}^h \right\|_1,$$

we get

$$\operatorname{DV}_{\alpha}^{q,h}(\nabla^h \mathbf{z}_0^h) = \inf_{\substack{\mathbf{z}_j^h \in \mathbb{R}^{|\mathbb{X}_{\ell}^{j,h}|} \\ j=1, \dots, q-1 \\ \mathbf{z}_0^h = \mathbf{u}^h}} \left(\sum_{j=1}^{q-1} \alpha_{q-j} \left\| (\mathcal{W}^j)^T \mathbf{M}_j^h \mathcal{W}^j \nabla^h \mathbf{z}_{j-1}^h - \mathbf{z}_j^h \right\|_1 \right) + \alpha_0 \left\| \mathbf{M}_q^h \mathcal{W}^q \nabla^h \mathbf{z}_{q-1}^h \right\|_1,$$

and thus, with $\mathcal{K}_{j,j}^h$ as in (4.4), we conclude

$$\operatorname{TDV}_{\alpha}^{q,h}(\mathbf{u}^h, \mathcal{M}^h) = \inf_{\substack{\mathbf{z}_j^h \in \mathbb{R}^{|\mathbb{X}_{\ell}^{j,h}|} \\ j=1, \dots, q \\ \mathbf{z}_0^h = \mathbf{u}^h, \mathbf{z}_q^h = \mathbf{0}}} \left(\sum_{j=1}^q \alpha_{q-j} \left\| \mathcal{K}_{j,j}^h \mathbf{z}_{j-1}^h - \mathbf{z}_j^h \right\|_1 \right).$$

A continuous version of (4.3) also holds. This is proved in the second part of this work [42].

The characterisation of $\text{TDV}_{\alpha_q}^{q,h}$ in (4.3) is fundamental for writing a suitable primal-dual algorithm for the minimization problem in (1.13).

4.2. Discretised single minimization problems. Let $\mathbf{u}^{\diamond,h}$ be a given discrete imaging data. For a fixed order $q > 0$, let $\text{TDV}_{\alpha}^{q,h}(\mathbf{u}^h, \mathcal{M}^h)$ be decomposed as in (4.3), with $\mathcal{M}^h = (\mathbf{M}_j^h)_{j=1}^q$, $\alpha = (\alpha_j)_{j=0}^{q-1}$ and the $\|\cdot\|_1$ denoted in the discrete setting by $\|\mathbf{Z}\|_{2,1} = \sum_{i,j} \sqrt{\sum_{k=1}^s (\mathbf{Z}_k)_{i,j}^2}$ for a generic tensor-valued object $\mathbf{Z} = (\mathbf{Z}_k)_{k=1}^s$, with each $\mathbf{Z}_k \in \mathcal{T}^2(\mathbb{R}^{M \times N})$.

The discrete single minimization problems, for \mathbf{z}^h defined as in Section 3.2 read as:

- for order $q = 1$, $\mathcal{M}^h = (\mathbf{M}_1^h)$, $\alpha = \alpha_0$, $\mathbf{z}^h = (z_0^h)$:

$$(4.5) \quad \min_{\mathbf{z}^h} \left(\alpha_0 \|\mathbf{M}_1^h \mathcal{W}^1 \nabla^h z_0^h\|_{2,1} + \frac{\eta}{2} \|\mathcal{S} z_0^h - z_0^{\diamond,h}\|_2^2 \right);$$

- for order $q = 2$, $\mathcal{M}_2^h = (\mathbf{M}_1^h, \mathbf{M}_2^h)$, $\alpha = (\alpha_0, \alpha_1)$, $\mathbf{z}^h = (z_0^h, z_1^h)$:

$$(4.6) \quad \min_{\mathbf{z}^h} \left(\alpha_1 \|(\mathcal{W}^1)^T \mathbf{M}_1^h \mathcal{W}^1 \nabla^h z_0^h - z_1^h\|_{2,1} + \alpha_0 \|\mathbf{M}_2^h \mathcal{W}^2 \nabla^h z_1^h\|_{2,1} + \frac{\eta}{2} \|\mathcal{S} z_0^h - z_0^{\diamond,h}\|_2^2 \right);$$

- for order $q = 3$, $\mathcal{M}_3^h = (\mathbf{M}_1^h, \mathbf{M}_2^h, \mathbf{M}_3^h)$, $\alpha_3 = (\alpha_0, \alpha_1, \alpha_2)$, $\mathbf{z}^h = (z_0^h, z_1^h, z_2^h)$:

$$(4.7) \quad \min_{\mathbf{z}^h} \left(\alpha_2 \|(\mathcal{W}^1)^T \mathbf{M}_1^h \mathcal{W}^1 \nabla^h z_0^h - z_1^h\|_{2,1} + \alpha_1 \|(\mathcal{W}^2)^T \mathbf{M}_2^h \mathcal{W}^2 \nabla^h z_1^h - z_2^h\|_{2,1} + \alpha_0 \|\mathbf{M}_3^h \mathcal{W}^3 \nabla^h z_2^h\|_{2,1} + \frac{\eta}{2} \|\mathcal{S} z_0^h - z_0^{\diamond,h}\|_2^2 \right).$$

For a fixed $q > 0$, we aim to provide a more concise formulation of (4.5)–(4.7). Let \mathbf{z}^h be as above and $\mathcal{K}^h = (\mathcal{K}_{j,\ell}^h)_{j,\ell=1}^q$ be a matrix of operators associated to $\text{TDV}_{\alpha}^{q,h}$ and defined as

$$(4.8) \quad \mathcal{K}^h = \begin{pmatrix} \mathcal{K}_{1,1}^h & -\mathbf{I} & \mathbf{0} & \dots & \dots & \dots & \mathbf{0} \\ \mathbf{0} & \mathcal{K}_{2,2}^h & -\mathbf{I} & \mathbf{0} & & & \vdots \\ \vdots & \ddots & \ddots & \ddots & \ddots & & \vdots \\ \vdots & & \mathbf{0} & \mathcal{K}_{j,j}^h & -\mathbf{I} & \mathbf{0} & \vdots \\ \vdots & & & \ddots & \ddots & \ddots & \mathbf{0} \\ \vdots & & & & \mathbf{0} & \mathcal{K}_{q-1,q-1}^h & -\mathbf{I} \\ \mathbf{0} & \dots & \dots & \dots & \dots & \mathbf{0} & \mathcal{K}_{q,q}^h \end{pmatrix},$$

i.e. with $\mathcal{K}_{j,\ell}^h = \mathbf{0}$ if $\ell \neq \{j, j+1\}$, $\mathcal{K}_{j,j+1}^h = -\mathbf{I}$ and as $\mathcal{K}_{j,j}^h$ in (4.4) for each $j = 1, \dots, q$. Then, solving (4.1) is equivalent to solving for $\mathbf{z}^h = (z_0^h, \dots, z_{q-1}^h)$, with $z_0^h = \mathbf{u}^h$, the problem:

$$(4.9) \quad \mathbf{u}^* \in \arg \min_{\mathbf{u}^h \in \mathbb{R}^{|\Omega^h|}} \inf_{\mathbf{z}^h} \sum_{j=1}^q \alpha_{q-j} \left\| \sum_{\ell=1}^q \mathcal{K}_{j,\ell}^h z_{\ell-1}^h \right\|_{2,1} + \frac{\eta}{2} \|\mathcal{S} z_0^h - \mathbf{u}^{\diamond,h}\|_2^2.$$

By duality of the $\|\cdot\|_{2,1}$ norm and recalling that \mathbf{w}^h is the dual vector defined in [Section 3.2](#), we rewrite (4.9) into a saddle-point minimization problem:

$$(4.10) \quad \min_{\mathbf{z}^h} \max_{\mathbf{w}^h} \left\langle \sum_{\ell=1}^q \mathcal{K}_{j,\ell}^h \mathbf{z}_{\ell-1}^h, \mathbf{w}_j^h \right\rangle - \sum_{j=1}^q \delta_{\{\|\cdot\|_{2,\infty} \leq \alpha_{q-j}\}}(\mathbf{w}_j^h) + \frac{\eta}{2} \|\mathcal{S}\mathbf{z}_0^h - \mathbf{u}^{\diamond,h}\|_2^2,$$

or, in short notation:

$$(4.11) \quad \min_{\mathbf{z}^h} \max_{\mathbf{w}^h} \langle \mathcal{K}^h \mathbf{z}^h, \mathbf{w}^h \rangle - F^*(\mathbf{w}^h) + G(\mathbf{z}^h),$$

where $G(\mathbf{z}^h)$ is a partially strongly convex term, since it can be seen as $G(\mathbf{z}^h) = G_0(\mathcal{P}\mathbf{z}^h)$ for the projection \mathcal{P} of \mathbf{z}^h onto the subspace of \mathbf{z}_0^h and with G_0 being strongly convex, and where

$$F^*(\mathbf{w}^h) = \sum_{j=1}^q \delta_{\{\|\cdot\|_{2,\infty} \leq \alpha_{q-j}\}}(\mathbf{w}_j^h),$$

and

$$G(\mathbf{z}^h) = G_0(\mathcal{P}\mathbf{z}^h) = \frac{\eta}{2} \left\| \mathcal{P} \begin{pmatrix} \mathbf{z}_0^h \\ \mathbf{z}_1^h \\ \vdots \\ \mathbf{z}_q^h \end{pmatrix} - \begin{pmatrix} \mathbf{u}^{\diamond,h} \\ \mathbf{0} \\ \vdots \\ \mathbf{0} \end{pmatrix} \right\|_2^2 \quad \text{with } \mathcal{P} = \begin{pmatrix} \mathcal{S} & \mathbf{0} & \dots & \mathbf{0} \\ \mathbf{0} & \mathbf{0} & \dots & \mathbf{0} \\ \vdots & \vdots & \ddots & \mathbf{0} \\ \mathbf{0} & \mathbf{0} & \dots & \mathbf{0} \end{pmatrix},$$

and $\mathcal{P}\mathbf{z}^h = (\mathcal{S}\mathbf{z}_0^h, \mathbf{0}, \dots, \mathbf{0})^\top$.

4.3. Proximal operators. We aim to solve the saddle point problem (4.11) with a Primal-Dual Hybrid Gradient (PDHG) algorithm. We need the proximal operators of F^* and G .

The proximal map of F^* evaluated at a point $\widehat{\mathbf{w}}^h$ is the sum of the projections onto the respective polar balls since F^* is fully separable¹,

$$\mathbf{prox}_{\sigma F^*}(\widehat{\mathbf{w}}^h) = \sum_{j=1}^q \mathbf{prox}_{\sigma F^*}(\widehat{\mathbf{w}}_j^h), \quad \text{with } \mathbf{prox}_{\sigma F^*}(\widehat{\mathbf{w}}_j^h) = \frac{\widehat{\mathbf{w}}_j^h}{\max\left(1, \alpha_{q-j}^{-1} \|\widehat{\mathbf{w}}_j^h\|_2\right)}.$$

The proximal map of G should be evaluated at a point $\widehat{\mathbf{z}}^h$. Recalling that $\mathbf{z}_0^h = \mathbf{u}^h$ and that \mathbf{z} is as in [Section 3.2](#), we have:

$$(4.12) \quad \begin{aligned} \mathbf{prox}_{\tau G}(\widehat{\mathbf{z}}^h) &= \arg \min_{\mathbf{z}^h} \left(\frac{\eta}{2} \left\| \begin{pmatrix} \mathcal{S}\mathbf{z}_0^h - \mathbf{u}^{\diamond,h} \\ \mathbf{0} \\ \vdots \\ \mathbf{0} \end{pmatrix} \right\|_2^2 + \frac{1}{2\tau} \left\| \begin{pmatrix} \mathbf{z}_0^h \\ \mathbf{z}_1^h \\ \vdots \\ \mathbf{z}_q^h \end{pmatrix} - \begin{pmatrix} \widehat{\mathbf{z}}_0^h \\ \widehat{\mathbf{z}}_1^h \\ \vdots \\ \widehat{\mathbf{z}}_q^h \end{pmatrix} \right\|_2^2 \right) \\ &= \begin{pmatrix} \arg \min_{\mathbf{z}_0^h \in \mathbb{R}^{|\Omega^h|}} \left(\frac{\eta}{2} \|\mathcal{S}\mathbf{z}_0^h - \mathbf{u}^{\diamond,h}\|_2^2 + \frac{1}{2\tau} \|\mathbf{z}_0^h - \widehat{\mathbf{z}}_0^h\|_2^2 \right) \\ \widehat{\mathbf{z}}_1^h \\ \vdots \\ \widehat{\mathbf{z}}_q^h \end{pmatrix}. \end{aligned}$$

¹meaning that F^* is a function that can be written as a sum of functions in disjoint sets of variables.

Let us focus on the first component of $\mathbf{prox}_{\tau G}$, in (4.12): we have to solve

$$\arg \min_{\mathbf{z}_0^h \in \mathbb{R}^{|\Omega^h|}} \frac{\eta}{2} \|\mathcal{S}\mathbf{z}_0^h - \mathbf{u}^{\diamond, h}\|_2^2 + \frac{1}{2\tau} \|\mathbf{z}_0^h - \widehat{\mathbf{z}}_0^h\|_2^2,$$

whose minimum is achieved by a \mathbf{z}_0^h that solves, for \mathcal{S}^* adjoint of \mathcal{S} ,

$$\begin{aligned} \tau\eta\mathcal{S}^*(\mathcal{S}\mathbf{z}_0^h - \mathbf{u}^{\diamond, h}) + (\mathbf{z}_0^h - \widehat{\mathbf{z}}_0^h) &= 0 \\ (\mathbf{I} + \tau\eta\mathcal{S}^*\mathcal{S})\mathbf{z}_0^h - \tau\eta\mathcal{S}^*\mathbf{u}^{\diamond, h} - \widehat{\mathbf{z}}_0^h &= 0 \\ (\mathbf{I} + \tau\eta\mathcal{S}^*\mathcal{S})\mathbf{z}_0^h - \tau\eta\mathcal{S}^*\mathbf{u}^{\diamond, h} - \widehat{\mathbf{z}}_0^h + \tau\eta\mathcal{S}^*\mathcal{S}\widehat{\mathbf{z}}_0^h - \tau\eta\mathcal{S}^*\mathcal{S}\widehat{\mathbf{z}}_0^h &= 0 \\ (\mathbf{I} + \tau\eta\mathcal{S}^*\mathcal{S})(\mathbf{z}_0^h - \widehat{\mathbf{z}}_0^h) &= \tau\eta\mathcal{S}^*(\mathbf{u}^{\diamond, h} - \mathcal{S}\widehat{\mathbf{z}}_0^h). \end{aligned}$$

Thus, the first component of $\mathbf{prox}_{\tau G}(\widehat{\mathbf{z}}^h)$, that is $\mathbf{prox}_{\tau G_0}(\mathcal{P}\widehat{\mathbf{z}}^h)$, is

$$\mathbf{z}_0^h = \widehat{\mathbf{z}}_0^h + (\mathbf{I} + \tau\eta\mathcal{S}^*\mathcal{S})^{-1}\tau\eta\mathcal{S}^*(\mathbf{u}^{\diamond, h} - \mathcal{S}\widehat{\mathbf{z}}_0^h).$$

Note that for the Rudin-Osher-Fatemi denoising problem we have $\mathcal{S} = \mathbf{I}$, thus $\mathcal{S}^* = \mathbf{I}$, and the proximal map agrees with the one computed in [15, pag. 133].

4.4. Operator norm. Following the approach in [11, Section 4] and [15, Section 6.1], we estimate a bound on the norm of the linear operator $\nabla_{\mathcal{M}^h, \mathcal{W}}^{q, h}$ in (3.5) in view of the implementation of a suitable primal-dual algorithm. Let $\|\cdot\|$ be the operator norm, then for each $q = 1, \dots, Q$ we have

$$(4.13) \quad L_q^2 = \left\| \nabla_{\mathcal{M}^h, \mathcal{W}}^{q, h} \right\|^2 = \left\| \operatorname{div}_{\mathcal{M}^h, \mathcal{W}}^{q, h} \right\|^2 = \sup_{\Psi^h \in \mathcal{Y}_{\mathcal{M}^h, \alpha}^{q, h}} \frac{\left\| \operatorname{div}_{\mathcal{M}^h, \mathcal{W}}^{q, h} \Psi^h \right\|_2^2}{\left\| \Psi^h \right\|_2^2}.$$

In the two-dimensional setting, when $q = 1$ then $\operatorname{div}_{\mathcal{M}^h, \mathcal{W}}^{1, h} \Psi^h$ in (4.13) reduces to

$$\operatorname{div}_{\mathcal{M}^h, \mathcal{W}}^{1, h} \Psi^h = \operatorname{div}^{1, h}((\mathbf{M}_1^h \mathcal{W}^1)^T \Psi^h),$$

and by applying the finite difference scheme in (3.3), from $\|\nabla\| \leq \sqrt{8}h^{-1}$ we estimate:

$$\begin{aligned} L_1^2 &= \left\| \operatorname{div}_{\mathcal{M}^h, \mathcal{W}}^{1, h} \Psi^h \right\|^2 = \operatorname{div}_{\mathcal{M}^h, \mathcal{W}}^{1, h} \Psi^h \cdot \operatorname{div}_{\mathcal{M}^h, \mathcal{W}}^{1, h} \Psi^h \\ &= \operatorname{div}((\mathbf{M}_1^h \mathcal{W}^1)^T \Psi^h) \cdot \operatorname{div}((\mathbf{M}_1^h \mathcal{W}^1)^T \Psi^h) \\ &= \mathbf{M}_1^h \mathcal{W}^1 \nabla \otimes \operatorname{div}((\mathbf{M}_1^h \mathcal{W}^1)^T \Psi^h) \cdot \Psi^h \leq \frac{8}{h^2} \|\mathbf{M}_1^h \mathcal{W}^1\|_F^2 \|\Psi^h\|_2^2. \end{aligned}$$

For a fixed q , since it holds

$$\left\| (\mathcal{W}^j)^T \mathbf{M}_j^h \mathcal{W}^j \right\|_F = \left\| ((\mathcal{W}^j)^T \mathbf{M}_j^h \mathcal{W}^j)^T \right\|_F, \quad \text{for each } j = 1, \dots, q,$$

then the operator norm L_q is estimated via

$$(4.14) \quad L_q^2 \leq (8h^{-2})^q \prod_{j=1}^q \left\| (\mathcal{W}^j)^T \mathbf{M}_j^h \mathcal{W}^j \right\|_2^2.$$

Remark 4.1. Since \mathcal{W} is made by partition of unit transfer operators and $\left\| \mathbf{M}_j^h \right\|_2 \leq 1$ by construction, we can estimate the right-hand side of (4.14) as:

$$L_q^2 \leq (8h^{-2})^q,$$

which agrees with the classic isotropic setting given by the choices $\mathbf{M}_j^h = \mathbf{I}$ without the use of \mathcal{W}^j for every $j = 1, \dots, q$. Indeed, we have $L^2 \leq 8h^{-2}$ for TV and $L^2 \leq 64h^{-4}$ for TGV_α^2 .

4.5. Primal-Dual Hybrid Gradient algorithm. Now we are ready for solving (4.11) with a Primal-Dual Hybrid Gradient (PDHG) algorithm following [15]. Let q be fixed and $L_q = \|\mathcal{K}\|$ be the operator norm as in Section 4.4, i.e. $L_q := \sup_{\mathbf{z}} \{\|\mathcal{K}\mathbf{z}\|_2 \text{ s.t. } \|\mathbf{z}\|_2 \leq 1\}$, and let $\tau, \sigma > 0$, $\omega \in [0, 1]$ be fixed, such that $\tau\sigma L_q^2 < 1$. Then the PDHG algorithm [15, Algorithm 1] reads as the iteration of

$$(4.15) \quad \begin{aligned} \mathbf{w}^{n+1,h} &= \mathbf{prox}_{\sigma F^*}(\mathbf{w}^{n,h} + \sigma \mathcal{K}^h \bar{\mathbf{z}}^{n,h}); \\ \mathbf{z}^{n+1,h} &= \mathbf{prox}_{\tau G}(\mathbf{z}^{n,h} - \tau (\mathcal{K}^h)^* \mathbf{w}^{n+1,h}); \\ \bar{\mathbf{z}}^{n+1,h} &= \mathbf{z}^{n+1,h} + \omega(\mathbf{z}^{n+1,h} - \mathbf{z}^{n,h}), \end{aligned}$$

where we denoted with an index n the iterations, starting from admissible $\mathbf{z}^{0,h}$ and $\mathbf{w}^{0,h}$. The final solution is achieved by $\mathbf{u}^* = \mathbf{z}_0^{n+1,h}$. Compare Algorithm 4.1 for details.

Acceleration. If $\mathcal{S} = \mathbf{I}$ and only the first order regulariser is involved ($Q = 1$) then the fidelity term G is strongly convex with convexity parameter η (since it does not involve the terms of \mathbf{z}^h related to the derivatives of order greater than 1) and the dual problem is smooth. Therefore, it is possible to accelerate the PDHG algorithm with [15, Algorithm 2]: we can take $\tau_0\sigma_0 L_q^2 \leq 1$ and update $\tau_n, \sigma_n, \omega_n$ by taking L_G as the Lipschitz constant of G , $\tau_0 = L_q^{-1}$ and $\gamma = 0.5L_G^{-1}$, with the update rule in (4.15) before $\bar{\mathbf{z}}^{n+1,h}$ reading as

$$\omega_n = (1 + 2\gamma\tau_n)^{-0.5}; \tau_{n+1} = \omega_n\tau_n; \sigma_{n+1} = \sigma_n\omega_n^{-1}.$$

When $\mathcal{S} = \mathbf{I}$ and $Q > 1$ then G is only partially strongly convex and one can use either [15, Algorithm 1] or the acceleration proposed in [55]. In any case, when \mathcal{S} makes G not strongly convex then the use of [15, Algorithm 1] is recommended: in such case, σ_n and τ_n are fixed a-priori, e.g. the authors in [32] adopted the parameters $\sigma_n = \tau_n = 1/\sqrt{12}$ for the second-order regulariser TGV^2 and for a grid of grid-size $h = 1$.

4.6. Primal-Dual Gap. As exit condition for the primal-dual algorithm of the $\text{TDV}_\alpha^{q,h} - \text{L}^2$ minimisation problem, it is possible to either define a maximum number of iterations to reach or to impose a threshold for the primal-dual gap, defined for the current solutions $\bar{\mathbf{z}}$ and $\bar{\mathbf{w}}$ as

$$(4.16) \quad \begin{aligned} \text{pdhg_gap}(\bar{\mathbf{z}}, \bar{\mathbf{w}}) &= \text{TDV}_\alpha^{q,h}(\bar{\mathbf{z}}_0, \mathcal{M}^h) + \frac{\eta}{2} \|\bar{\mathbf{z}}_0 - \mathbf{u}^{\diamond,h}\|_2^2 \\ &+ \sum_{j=1}^q \delta_{\{\|\cdot\|_{2,\infty} \leq \alpha_{q-j}\}}(\bar{\mathbf{w}}_j) + \frac{\eta}{2} \|(\mathcal{K}^h)^* \bar{\mathbf{w}}\|_2^2 - \eta \langle (\mathcal{K}^h)^* \bar{\mathbf{w}}, \begin{pmatrix} \mathbf{z}_0^\diamond \\ \mathbf{0} \\ \vdots \\ \mathbf{0} \end{pmatrix} \rangle. \end{aligned}$$

Algorithm 4.1 PDHG algorithm for the minimization model in Equation (4.11)

Parameters for the model : $q > 0, \eta > 0$ and $\alpha = (\alpha_j)_{j=0}^{q-1}$.

Operators needed : $\mathcal{K}^h, \mathcal{S}$.

Parameters for primal-dual: $\sigma_0, \tau_0, \omega_0$ such that $\sigma_0 \tau_0 L_q^2 < 1$ for $L_q = \|\mathcal{K}^h\|, \gamma > 0$.

Variables to initialize : $\mathbf{z}^{0,h} = (\mathbf{z}_{j-1}^{0,h})_{j=1}^Q, \mathbf{w}^{0,h} = (\mathbf{w}_j^{0,h})_{j=1}^q$.

Function PrimalDual ($\mathbf{u}^{\diamond,h}, \mathcal{K}^h, \alpha, \eta$):

```

while stopping criterion is not satisfied do
    // Dual problem
    for  $j = 1, \dots, q-1$  do
         $\mathbf{w}_j^{n,h} \leftarrow \mathbf{w}_j^{n,h} + \sigma_n (\mathcal{K}_{j,j}^h \bar{\mathbf{z}}_{j-1}^{n,h} - \bar{\mathbf{z}}_j^{n,h});$  // update the dual (inner)
         $\mathbf{w}_j^{n+1,h} = \mathbf{w}_j^{n,h} / \max(1, \alpha_{q-j}^{-1} \|\mathbf{w}_j^{n,h}\|_2);$  // proximal operator of  $F^*$  (inner)
    end
     $\mathbf{w}_q^{n,h} \leftarrow \mathbf{w}_q^{n,h} + \sigma_n \mathcal{K}_{q,q}^h \bar{\mathbf{z}}_{q-1}^{n,h};$  // update the dual (outer)
     $\mathbf{w}_q^{n+1,h} = \mathbf{w}_q^{n,h} / \max(1, \alpha_0^{-1} \|\mathbf{w}_q^{n,h}\|_2);$  // proximal operator of  $F^*$  (outer)
    // Primal problem
    for  $j = 2, \dots, q$  do
         $\mathbf{z}_{j-1}^{n,h} \leftarrow \mathbf{z}_{j-1}^{n,h} - \tau_n (\mathcal{K}_{j,j}^h)^* \mathbf{w}_j^{n+1,h} - \mathbf{w}_{j-1}^{n+1,h};$  // update the primal (inner)
         $\mathbf{z}_{j-1}^{n+1,h} = \mathbf{z}_{j-1}^{n,h};$  // proximal operator of  $G$  (inner)
    end
     $\mathbf{z}_0^{n,h} \leftarrow \mathbf{z}_0^{n,h} - \tau_n ((\mathcal{K}_{1,1}^h)^* \mathbf{w}_1^{n+1,h});$  // update the primal (outer)
     $\mathbf{z}_0^{n+1,h} = \mathbf{z}_0^{n,h} + (\mathbf{I} + \tau \eta \mathcal{S}^* \mathcal{S})^{-1} \tau \eta \mathcal{S}^* (\mathbf{u}^{\diamond,h} - \mathcal{S} \mathbf{z}_0^{n,h});$  // proximal operator of  $G$  (outer)
    // Parameters update
     $\omega_n = \omega_0; \tau_{n+1} = \tau_0; \sigma_{n+1} = \sigma_0;$  // or update  $\omega_n, \tau_n, \sigma_n$  if acceleration is possible
    // Extrapolation step
     $\bar{\mathbf{z}}^{n+1,h} = \mathbf{z}^{n+1,h} + \omega_n (\mathbf{z}^{n+1,h} - \mathbf{z}^{n,h});$ 
end
return  $\mathbf{u}^* = \mathbf{z}_0^{n+1,h}$ .

```

4.7. Joint minimisation problem. In the continuous setting and for any fixed $q > 0$, the particular choice of $\mathcal{M} = (\mathbf{I}, \dots, \mathbf{I}, \mathbf{M})$ and $\alpha = (\alpha_{q,0}, +\infty, \dots, +\infty)$ deserves a separate discussion. Indeed, the decomposition of TDV_{α}^q in the continuous setting results as

$$\text{TDV}_{\alpha}^q(u, \mathcal{M}) = \alpha_0 \|\mathbf{M} \nabla \mathbf{z}_{q-1}\|_{2,1} + \sum_{j=1}^{q-1} +\infty \|\nabla \mathbf{z}_{j-1} - \mathbf{z}_j\|_{2,1},$$

in which the sparsity of the inner order of derivatives would not be fully exploited due to the weight $+\infty$. The above decomposition is equivalent to impose $\mathbf{z}_j = \nabla \mathbf{z}_{j-1}$ for any $j = 1, \dots, q-1$, resulting in $\text{TDV}_{\alpha}^q(u, \mathcal{M}) \equiv \|\mathbf{M} \nabla^q u\|_{2,1}$. As discussed in Remark 3.4, in this case the usage of the transfer operators in the discrete setting and for the inner order of

derivates is useless and we can therefore discretise the above regulariser as

$$\text{TDV}_{\alpha}^{q,h}(\mathbf{u}^h, \mathcal{M}^h) \equiv \alpha_0 \|\mathbf{M}^h \mathcal{W}^q \nabla^q \mathbf{u}^h\|_{2,1}.$$

In our applications, we will mainly focus on the effect of weighting the highest order derivative by means of taking the exact inner derivatives, but combined jointly with regularisers $\text{TDV}_{\alpha_q}^q$ for different $q > 0$, i.e. we aim to solve in the discrete setting

$$(4.17) \quad \mathbf{u}^* \in \arg \min_{\mathbf{u}^h \in \mathbb{R}^{|\Omega^h|}} \sum_{q=1}^Q \text{TDV}_{\alpha_q}^{q,h}(\mathbf{u}^h, \mathcal{M}_q^h) + \frac{\eta}{2} \|\mathcal{S}\mathbf{u}^h - \mathbf{u}^{\diamond,h}\|_2^2,$$

with $\mathcal{M}_q^h = (\mathbf{I}, \dots, \mathbf{I}, \mathbf{M}_q^h)$ and $\alpha_q = (\alpha_{q,0}, +\infty, \dots, \infty)$ for each $q = 1, \dots, Q$, leading to

$$\mathbf{u}^* \in \arg \min_{\mathbf{u}^h \in \mathbb{R}^{|\Omega^h|}} \left(\sum_{q=1}^Q \alpha_{q,0} \|\mathbf{M}_q^h \mathcal{W}^q \nabla \otimes \nabla^{q-1} \mathbf{u}^h\|_{2,1} + \frac{\eta}{2} \|\mathcal{S}\mathbf{u}^h - \mathbf{u}^{\diamond,h}\|_2^2 \right).$$

Then it is possible to reduce [Algorithm 4.1](#) to [Algorithm 4.2](#), where the accelerated PDHG [[15](#), [Algorithm 2](#)] can be used for any choice of \mathcal{S} that makes G strongly convex.

5. Imaging Denoising. In what follows we demonstrate the performance of the introduced regulariser $\text{TDV}_{\alpha_q}^q$ for the applications of image denoising. We focus in particular on the cases $q = 1, 2, 3$ for the single [\(4.1\)](#) and joint minimisation model [\(4.17\)](#). Results are computed on a standard laptop (MATLAB R2019a, MacBook Pro 13", 2.9 GHz Intel Core i5, 8 GB 1867 MHz DDR3). The code is freely available at the authors' webpage².

Let $\Omega \subset \mathbb{R}^2$, $u : \Omega \rightarrow \mathbb{R}$ be a grey-scale image (colour images $\mathbf{u} : \Omega \rightarrow \mathbb{R}^3$ are considered one colour channel at time), $\mathbf{v} : \Omega \rightarrow \mathbb{R}^2$ a field with $\|\mathbf{v}\|_2 = 1$ and u^{\diamond} a given noisy image.

5.1. Estimation of vector field \mathbf{v} . For estimating \mathbf{v} we use the following strategy. Let $\sigma, \rho > 0$. Let $\lambda_1(\mathbf{x}), \lambda_2(\mathbf{x})$ be such that $\lambda_1(\mathbf{x}) \geq \lambda_2(\mathbf{x})$, the ordered eigenvalues of

$$(5.1) \quad \mathbf{J}_{\rho}(u) := K_{\rho} * (\nabla u_{\sigma} \otimes \nabla u_{\sigma}) \quad \text{for } u_{\sigma} := K_{\sigma} * u,$$

and $\mathbf{e}_1, \mathbf{e}_2 \in \mathbb{R}^2$ the associated eigenvectors. Let $\tilde{\mathbf{v}}(\mathbf{x}) = \mathbf{e}_2(\mathbf{x})$ be the local direction of the anisotropy, corresponding to an approximation of $(\nabla^{\perp} u) / \|\nabla^{\perp} u\|$. In order to compute a vector field smoother than $\tilde{\mathbf{v}}$, we adopt a further regularisation step, similarly as in [[34](#)].

Let $w(\mathbf{x}) \in [0, 1]$. We aim to smooth the vector field where the anisotropy weight $w(\mathbf{x})$ is close to 0 while keeping the already computed vector field in regions with strong anisotropy. This is equivalent to solving the following problem:

$$(5.2) \quad \mathbf{v} = \arg \min_{\mathbf{t} \in \mathbb{R}^{|\Gamma^h|}} \frac{1}{2} \int_{\Omega} w(\mathbf{x}) \|\mathbf{t}(\mathbf{x}) - \tilde{\mathbf{v}}(\mathbf{x})\|_2^2 \, d\mathbf{x} + \frac{\gamma}{2} \int_{\Omega} \|\nabla \mathbf{t}(\mathbf{x})\|_2^2 \, d\mathbf{x}.$$

We use the local estimation of the anisotropy as weights $w(\mathbf{x})$, for $\varepsilon > 0$:

$$(5.3) \quad w(\mathbf{x}) = \frac{\lambda_1(\mathbf{x}) - \lambda_2(\mathbf{x})}{\lambda_1(\mathbf{x}) + \lambda_2(\mathbf{x}) + \varepsilon}.$$

²Code freely available at <https://github.com/simoneparisotto>

Algorithm 4.2 PDHG algorithm for the joint minimization reduced model in Equation (4.17)

Parameters for the model : $Q > 0, \eta > 0$ and $\mathbf{a} = (\alpha_{q,0})_{q=1}^Q$.

Operators needed : $\mathcal{K}^h = (\mathcal{K}_q^h)_{q=1}^Q$ where $\mathcal{K}_q^h = \mathbf{M}\mathcal{W}^q \nabla^{q,h}, \mathcal{S}$.

Parameters for primal-dual: $\sigma_0, \tau_0, \omega_0$ such that $\sigma_0 \tau_0 L_q^2 < 1$ for $L_q = \max_q \|\mathcal{K}_q^h\|$.

Variables to initialize : $\mathbf{u}^{0,h}, \mathbf{w}^{0,h} = (\mathbf{w}_{q,j}^{0,h})_{q,j=1}^Q$.

Function PrimalDual_reduced($\mathbf{u}^{\diamond,h}, \mathcal{K}^h, \mathbf{a}, \eta$):

```

while stopping criterion is not satisfied do
  // Dual problem
  for  $q = 1, \dots, Q$  do
     $\mathbf{w}_q^{n,h} \leftarrow \mathbf{w}_q^{n,h} + \sigma_n \mathcal{K}_q^h \bar{\mathbf{u}}^{n,h};$  // update the dual
     $\mathbf{w}_q^{n+1,h} = \mathbf{w}_q^{n,h} / \max(1, \alpha_{q,0}^{-1} \|\mathbf{w}_q^{n,h}\|_2);$  // proximal operator of  $F^*$ 
  end
  // Primal problem
   $\mathbf{u}^{n,h} \leftarrow \mathbf{u}^{n,h} - \tau_n \left( \sum_{q=1}^Q (\mathcal{K}_q^h)^* \mathbf{w}_q^{n+1,h} \right);$  // update the primal
   $\mathbf{u}^{n+1,h} = \mathbf{u}^{n,h} + (\mathbf{I} + \tau_n \mathcal{S}^* \mathcal{S})^{-1} \tau_n \mathcal{S}^* (\mathbf{u}^{\diamond,h} - \mathcal{S} \mathbf{u}^{n,h});$  // proximal operator of  $G$ 
  // Parameters update
   $\omega_n = \omega_0; \tau_{n+1} = \tau_0; \sigma_{n+1} = \sigma_0;$  // or update  $\omega_n, \tau_n, \sigma_n$  if acceleration is possible
  // Extrapolation step
   $\bar{\mathbf{u}}^{n+1,h} = \mathbf{u}^{n+1,h} + \omega_n (\mathbf{u}^{n+1,h} - \mathbf{u}^{n,h});$ 
end
return  $\mathbf{u}^* = \mathbf{u}^{n+1,h}$ .

```

We can use $w(\mathbf{x})$ also to vary locally $\mathbf{b} = (1, \beta(\mathbf{x}))$: we have already seen that the process is more isotropic as $\beta(\mathbf{x})$ is closer to 1. For this reason, a possible strategy to vary $\beta(\mathbf{x})$ is:

- first, estimate the anisotropy (values close to 1 correspond to isotropic regions) by:

$$(5.4) \quad \text{anisotropy}(\mathbf{x}) = 1 - w(\mathbf{x}),$$

- second, rescale in $[0, 1]$ to define β :

$$(5.5) \quad \beta(\mathbf{x}) = \frac{\text{anisotropy}(\mathbf{x}) - \min \text{anisotropy}(\mathbf{x})}{\max \text{anisotropy}(\mathbf{x}) - \min \text{anisotropy}(\mathbf{x})}.$$

With this strategy, the higher the image anisotropy the closer \mathbf{b} is to $(1, 0)$: in such cases strong directional structures are emphasised by our directional regulariser. Conversely, when $\mathbf{b} = (1, 1)$, isotropic smoothing is performed in flat regions. In the following, we will require that $\mathbf{b} = (1, \beta(\mathbf{x}))^T$ for every $\mathbf{x} \in \Omega$, thus

$$\mathbf{M} \nabla \otimes u(\mathbf{x}) = \mathbf{\Lambda}_{\mathbf{b}}(\mathbf{R}_{\theta})^T \nabla \otimes u(\mathbf{x}) = \begin{pmatrix} \nabla_{\mathbf{v}} u(\mathbf{x}) \\ \beta(\mathbf{x}) \nabla_{\mathbf{v}_{\perp}} u(\mathbf{x}) \end{pmatrix},$$

where \mathbf{v} is a given estimated field. Also, we may refine \mathbf{v} by updating the parameters (σ, ρ) so as to restart the denoising problem with a better estimation of the vector field.

5.2. Single minimisation model. Here we describe results with the single model $\text{TDV}_\alpha^q - L^2$ and fixed q to be chosen between 1, 2 and 3. We will explore all the possible combinations for $(\mathbf{M}_1, \dots, \mathbf{M}_q)$, where each \mathbf{M}_j will be either the identity \mathbf{I} or the anisotropic \mathbf{M} weights.

Numerical results. In [Figure 5.1](#) we report the results from the single $\text{TDV}_\alpha^q - L^2$ problem in [\(4.1\)](#), with fixed $q = 1, 2, 3$ and different choices for the anisotropy \mathcal{M}_q . To compute \mathbf{M} , we employ the spatially varying strategy based on the structure tensor eigen-decomposition described in [Section 5.1](#), with $(\sigma, \rho) = (2, 25)$ and $\mathbf{b} = (1, \beta(\mathbf{x}))$, where $\beta(\mathbf{x})$ follows from [\(5.3\)](#)–[\(5.5\)](#). In these experiments, we keep fixed $\eta = 1$, $\alpha_0 = 1$ and $\alpha_j = 1.25$ for $j = 1, \dots, q$ and we run [Algorithm 4.1](#) for `maxiter` = 1000. We compare our results with TGV_α^2 (with the same weights) from an online source³: our strategy is able to encode spatially varying directional information at all the derivative orders.

For the experiments of [Figure 5.2](#), we use the same anisotropy directions as in the experiments of [Figure 5.1](#), but we modulate the anisotropy weight β to test its impact on the result. More precisely, starting from the same anisotropy matrix \mathbf{M} of [Figure 5.1](#), we define two variants: $\mathbf{M}^{0.3}$ is obtained from \mathbf{M} by replacing $\mathbf{b} = (1, \beta(\mathbf{x}))$ with $\mathbf{b}_{0.3} = (1, 0.3\beta(\mathbf{x}))$, and $\mathbf{M}^{0.7}$ is obtained from \mathbf{M} by replacing \mathbf{b} with $\mathbf{b}_{0.7} = (1, 0.7\beta(\mathbf{x}))$. The results of [Figure 5.2](#) correspond to different anisotropic weighting of the first and second-order derivatives in the model $\text{TDV}_\alpha^2 - L^2$, see the figure caption for details. Interestingly, a better PSNR is obtained with two orders of derivation and the following strategies: if the first derivative is anisotropically weighted, it is better to opt for an isotropic weight of the second-order derivative. And if the first derivative is isotropically weighted, it is better to opt for a strong anisotropic weight of the second-order derivative. This latter case seems the best in terms of PSNR but, of course, sharper results are obtained when anisotropic weights are chosen. Obviously, the PSNR metric does not capture all aspects of an image and a visual evaluation by the end user remains necessary for the choice of the most suitable combination of derivative orders and anisotropic weights.

Remark 5.1. In our experiments we observed some checkerboard artifacts when employing strong anisotropies. This phenomenon has been attributed to spectral properties of finite differences [[59](#), [25](#)] and a non-negative stencil avoiding these issues has been introduced in [[25](#)] for the case of directional Hessian. We leave a generalization of [[25](#)] to our higher-order case for future work. The artifacts are not evident in the results of the next [Section 5.3](#), where the joint model and a specific choice of the weights help in producing better quality results.

Our approach has a reasonably large number of parameters depending on the noise level and the structural imaging information: the order of the derivatives, the spatially varying directional information from the structure tensor and the weights for the sparsity of the derivatives. This makes the model highly customisable, but also quite sensitive to parameters. In order to simplify the parameter choice, we detail in [Section 5.3](#) a simplified joint model with a suggested choice of parameters, particularly suited for images with large dominant structures, as well as for the reconstruction of images from scattered data, see [Section 6.2](#).

³Code available at www.gipsa-lab.grenoble-inp.fr/~laurent.condat/download/TGVdenoise.m

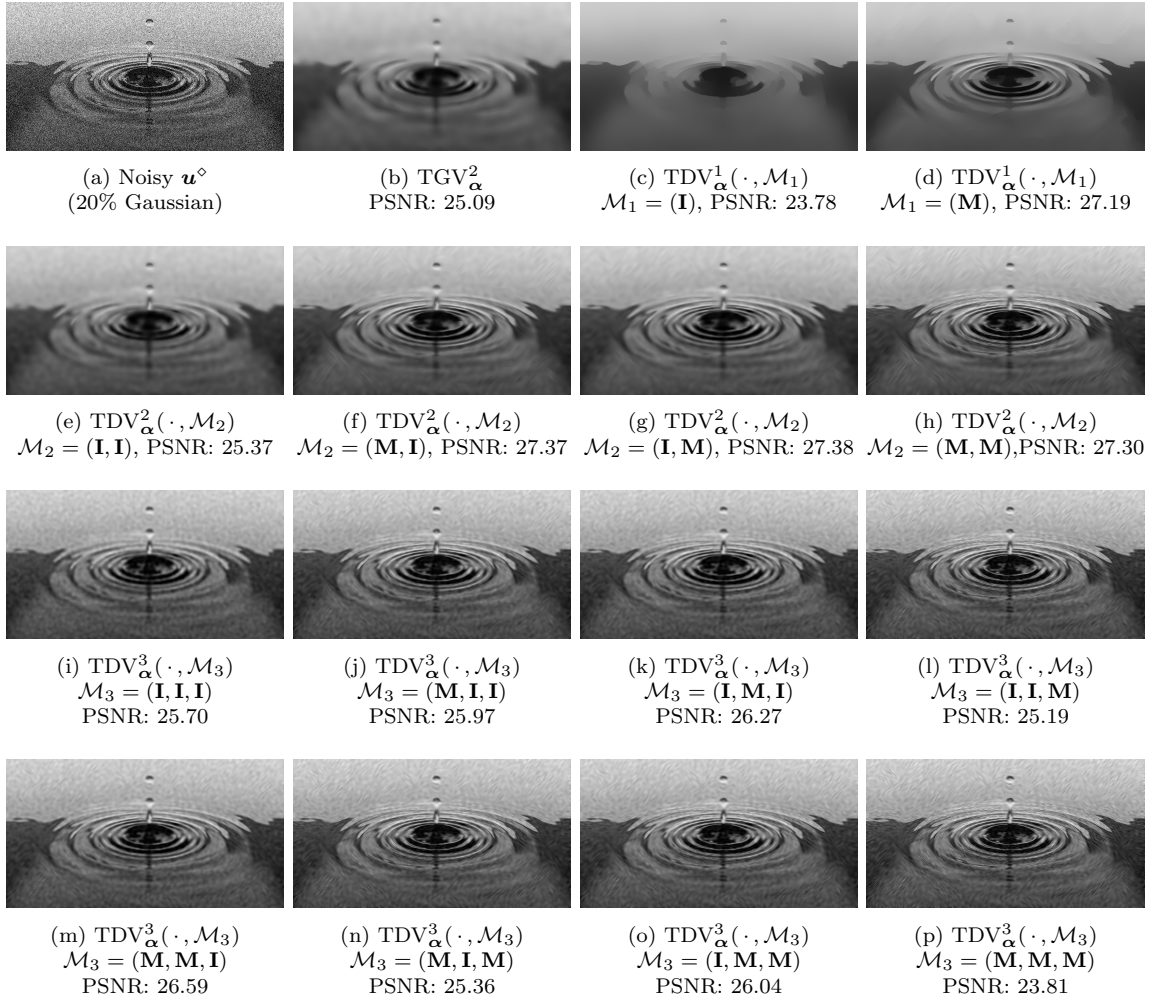


Figure 5.1: Here $\alpha = (\alpha_j)_{j=0}^{q-1}$ with $\alpha_0 = 1$ and $\alpha_j = 1.25$ for each $j > 0$, $(\sigma, \rho) = (2, 25)$ in the structure tensor computation, $\mathbf{b} = (1, \beta(\cdot))$ and fidelity $\eta = 1$.

5.3. Joint minimisation model. Following the comments in Remark 5.1, we now consider the joint model in (1.13) and described in Section 4.7 for $Q = 3$, with $\mathcal{M}_q = (\mathbf{I}, \dots, \mathbf{I}, \mathbf{M})$ and $\alpha_q = (\alpha_{q,0}, +\infty, \dots, +\infty)$ for each $q = 1, 2, 3$. Since we consider the denoising problem, we will make use of the identity operator $\mathcal{S} = \mathbf{I}$ in the fidelity term, aiming to solve:

$$(5.6) \quad u^* = \arg \min_{u \in \mathbb{R}^{|\Omega^h|}} \sum_{q=1}^Q \text{TDV}_{\alpha_q}^q(u, \mathcal{M}_q) + \frac{\eta}{2} \|u - u^\diamond\|_2^2.$$

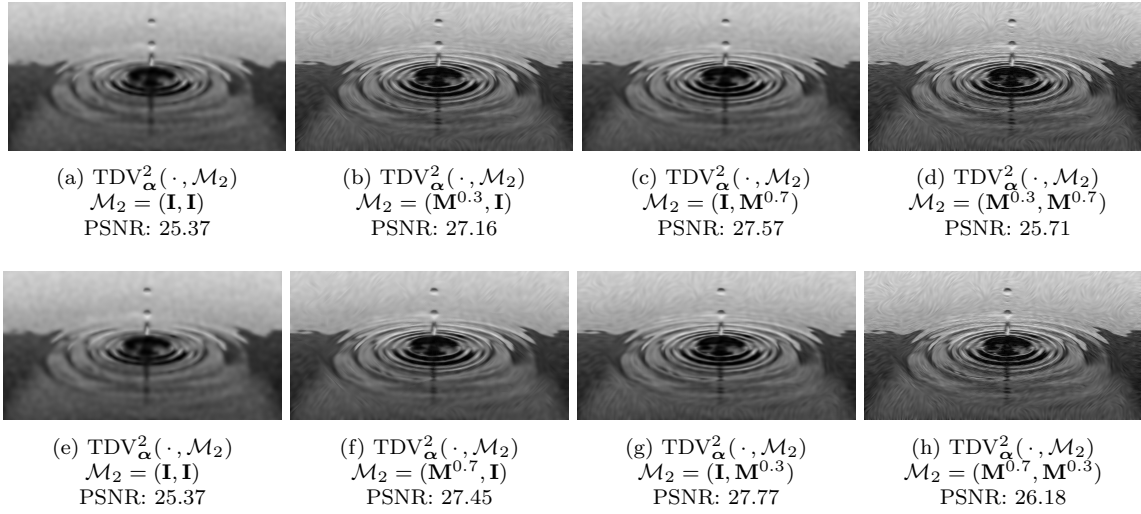


Figure 5.2: Here $\alpha = (\alpha_j)_{j=0}^{q-1}$ with $\alpha_0 = 1$ and $\alpha_j = 1.25$ for each $j > 0$, $(\sigma, \rho) = (2, 25)$, $\eta = 1$. Starting from the anisotropy matrix \mathbf{M} of Figure 5.1, we define two variants: $\mathbf{M}^{0.3}$ is obtained from \mathbf{M} by replacing $\mathbf{b} = (1, \beta(\mathbf{x}))$ with $\mathbf{b}_{0.3} = (1, 0.3\beta(\mathbf{x}))$, and $\mathbf{M}^{0.7}$ is obtained from \mathbf{M} by replacing \mathbf{b} with $\mathbf{b}_{0.7} = (1, 0.7\beta(\mathbf{x}))$. All other parameters are the same as in Figure 5.1. We report in Figures (5.2a–5.2d) the results obtained with four possible choices of \mathcal{M}_2 : (\mathbf{I}, \mathbf{I}) , $(\mathbf{M}^{0.3}, \mathbf{I})$, $(\mathbf{I}, \mathbf{M}^{0.7})$ and $(\mathbf{M}^{0.3}, \mathbf{M}^{0.7})$, respectively. The results in Figures (5.2e–5.2h) correspond to the choices (\mathbf{I}, \mathbf{I}) , $(\mathbf{M}^{0.7}, \mathbf{I})$, $(\mathbf{I}, \mathbf{M}^{0.3})$ and $(\mathbf{M}^{0.7}, \mathbf{M}^{0.3})$, respectively.

Thus, the denoising problem in equation (5.6) can be simplified as

$$(5.7) \quad u^* = \arg \min_{u \in \mathbb{R}^{|\Omega^h|}} \left(\sum_{q=1}^3 \alpha_{q,0} \|\mathbf{M}\mathcal{W}^q \nabla^q u\|_{2,1} + \frac{\eta}{2} \|u - u^\diamond\|_2^2 \right),$$

and solved via the primal-dual Algorithm 4.2 in which the computations for u and \mathbf{v} are performed alternately as described in Algorithm 5.1 so as to update the estimation of the directions \mathbf{v} . This updating strategy will allow a refinement for the computation of the directionality in images.

Numerical Results. We discuss denoising results obtained with Algorithm 5.1 and different denoising approaches (the non-local method BM3D with normal-complexity profile and prior knowledge of the standard deviation of the Gaussian noise [19] and the regularisers TV [45], TGV² [11], DTV and DTGV² [20]) for images with strong directional features. We run the primal-dual Algorithm 4.2 for 500 iterations and we restarted the Algorithm 5.1 once the first denoised image is computed which serves as an oracle for a better estimation of \mathbf{v} . We show results for grey-scale images in Figure 5.5 and for colour images Figures 5.7 and 5.8 and we discuss their PSNR.

Bamboo image. The grey-scale image in Figure 5.3a shows a strong directional direction. In Figure 5.3b it has been corrupted by 20% of Gaussian noise using the same random seed as

Algorithm 5.1 Discrete joint denoising problem (5.7)

Parameters for the model : $\mathbf{a} = (\alpha_{1,0}, \alpha_{2,0}, \alpha_{3,0})$, $\mathbf{b}^h = (\mathbf{I}, \mathbf{b}_2^h)$, $\eta > 0$, maxiter .

Parameters for \mathbf{v} : $\sigma_1, \rho_1 > 0$.

Function TDV_denoising($\mathbf{u}^{\diamond, h}$):

```

for  $k = 1, \dots, \text{maxiter}$  do
    [ $\mathbf{v}^{k+1, h}, \mathbf{b}^{k+1, h}$ ] = compute_v_and_b( $\mathbf{u}^k, \sigma_k, \rho_k$ ); // from (5.1)–(5.5)
     $\mathcal{K}^{k+1, h} = \text{build\_K}(\mathbf{a}, \mathbf{v}^{k+1, h}, \mathbf{b}^{k+1, h})$ ; // update  $\mathcal{K} = (\mathcal{K}_q^h)_{q=1}^Q$  with  $\mathcal{K}_q^h = \mathbf{M}\mathcal{W}^q \nabla^{q, h}$ 
     $\mathbf{u}^{k+1, h} = \text{PrimalDual\_reduced}(\mathbf{u}^{\diamond, h}, \mathcal{K}^{k+1, h}, \mathbf{a}, \eta)$ ; // restart denoising with new  $\mathcal{K}^{k+1}$ 
    [ $\sigma_{k+1}, \rho_{k+1}$ ] = update_sigmarho( $\sigma_k, \rho_k$ ); // new structure tensor parameters
end
return  $\mathbf{u}^{k+1, h}$ 

```

in [20], see Figure 5.3b. In Figure 5.3 we report the results from state of the art approaches, as reported in [20], where DTV and DTGV are considered with a single fixed choice of anisotropy direction and minor semi-axis (our parameter β). In Figures 5.3d and 5.3e the staircasing effect is visible as expected while Figure 5.3f and Figure 5.3g seem more promising, even if obtained with a single fixed direction only.

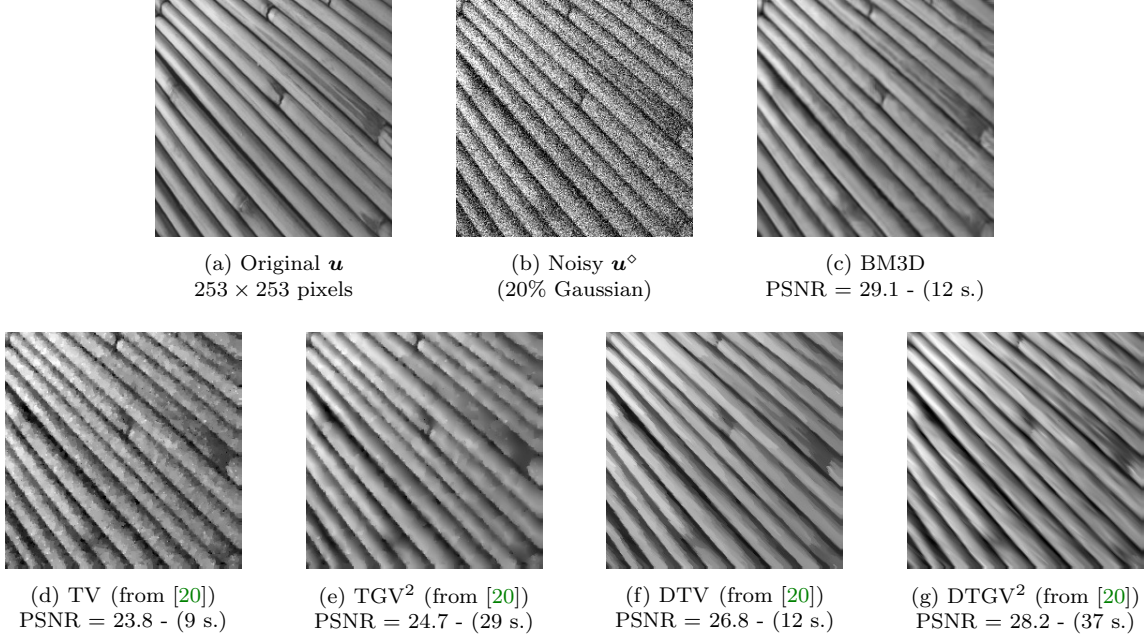


Figure 5.3: Denoising of bamboo grey-scale image: current approaches.

In our approach we vary the spatial directions estimating the vector field \mathbf{v} as described in (5.1)–(5.5) while we fix $\beta(\cdot)$, so as to fix the elliptic shape of the test functions. First, in Figure 5.4 we report the sensitivity to the parameter $\eta \in [0.24, 4]$ (with step-size increment of 0.25) for the first order TDV regulariser: from our experiments $\eta = 0.75$ produces a better

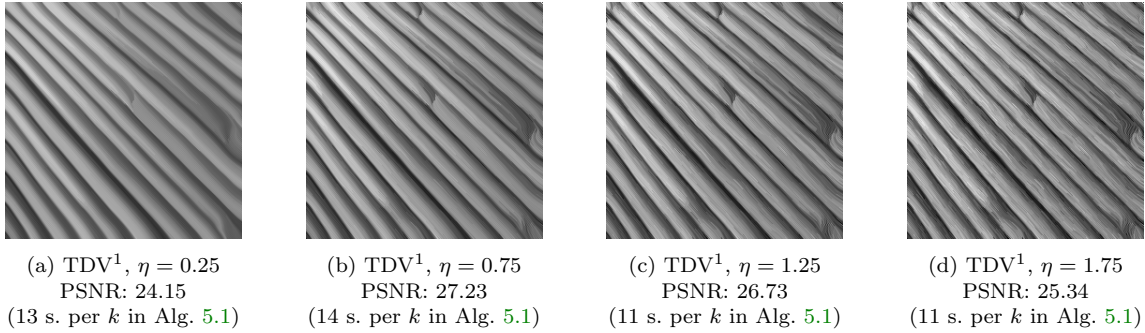


Figure 5.4: Denoising of Figure 5.3b for different fidelity weights η and first order TDV_α^1 regulariser with $\alpha = \alpha = 1$. Other parameters: Algorithm 5.1 with $\mathbf{b} = (1, 0.02)$ for the construction of \mathbf{M} , $(\sigma_1, \rho_1) = (1.8, 2.8)$ and $(\sigma_2, \rho_2) = (1, 1)$.

result than the first order regularisers, TV in Figure 5.3d and DTV in Figure 5.3f, and the second order TGV^2 in Figure 5.3e, showing less staircasing and directional artefacts. In this test, we fixed a-priori a number of parameters, i.e. $\mathbf{b} = (1, 0.02)$, $(\sigma_1, \rho_1) = (1.8, 2.8)$ and $(\sigma_2, \rho_2) = (1, 1)$ for the anisotropic structure in building \mathbf{M} and $\text{maxiter} = 2$ in Algorithm 5.1.

In Figure 5.5 we report the best results obtained with the same fixed choice of parameters but now with all the possible combinations of first, second and third order regularisers, as well as the sketch of the streamlines of \mathbf{v} in Figure 5.5a. We observed that the combination of the first and third order of regularisers outperforms the results from Figure 5.3. In the next paragraph we comment about further choices for the parameters.

Selection of parameters for the bamboo image. Let the choice of the regulariser orders \mathbf{a} and the maxiter in Algorithm 5.1 be fixed. We would like to estimate good parameters that directly affect the image reconstruction, namely the fidelity η , the directional information provided by (σ_1, ρ_1) of the structure tensor and β from $\mathbf{b} = (1, \beta)$ for the anisotropic shape of the test functions (assumed for now fixed all over the imaging domain). Unfortunately, the structure tensor depends on the intrinsic image content and standard deviation of the noise.

However, for $\eta = 3.5$ (among the $\eta \in [0.25, 4]$ tested) we obtained the best result for the combination of the first and third order regularisers, i.e. $\mathbf{a} = (1, 0, 1)$. Therefore we inspect more the PSNR obtained by fixing η, \mathbf{a} and by changing both $\beta \in \{0, 0.01, 0.02, 0.03\}$ and (σ_1, ρ_1) in the range between $(1.5, 3.5)$: results in Figure 5.6 show that the optimal parameters for this case are the ones producing Figure 5.5g as output. Other strategies for estimating the parameters, including η , would require to solve a bilevel problem, e.g. as in [21], or to solve the problem by updating the parameters with a greedy line-search approach onto many directional images, so as to extract a rule of thumb for the choice, e.g. as in [43].

A natural question now is whether allowing also $\beta(\cdot)$ to change in Ω improves the performances. We are going to answer this question in the next two experiments. However, since the scale of the directional texture in the next experiments are spatially different, we fix $\eta = 3.5$ and focus on the promising case of combination of first and third order regularisers, i.e. $\mathbf{a} = (1, 0, 1)$, with reasonable choice of (σ_1, ρ_1) .

Rainbow image. The rainbow in Figure 5.7a has been corrupted by 20% of Gaussian noise in each color channel, see Figure 5.7b. Due to the particular structure of the image, an isotropic

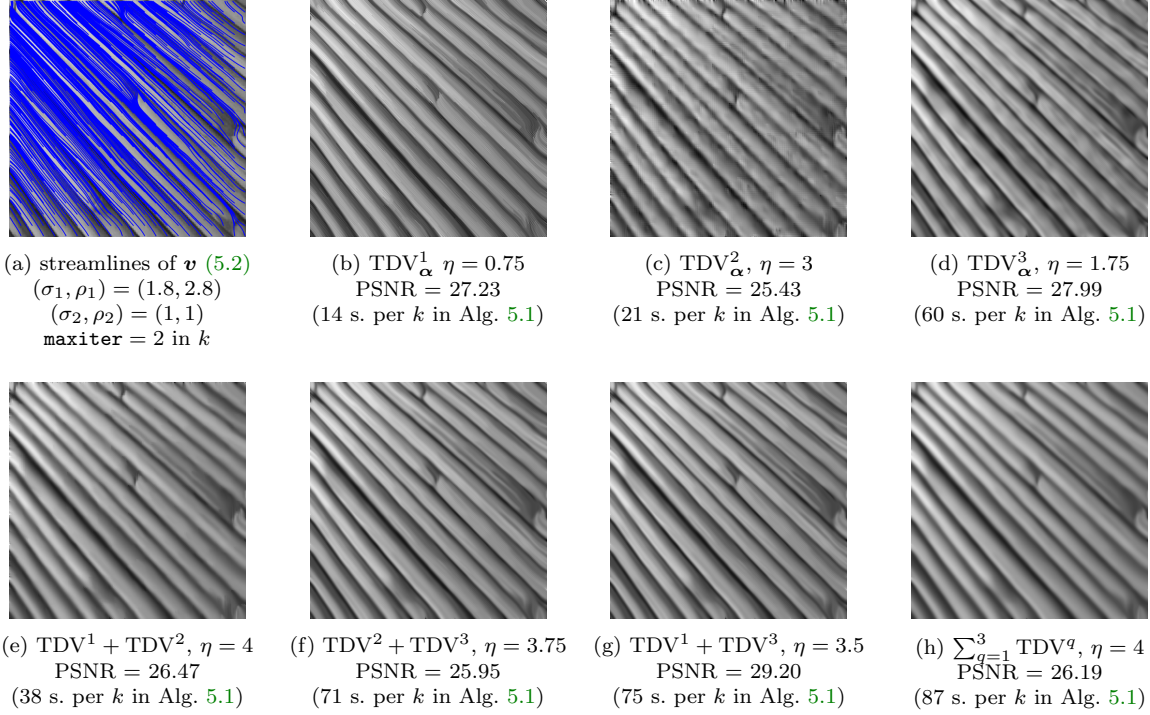


Figure 5.5: Denoising of Figure 5.3b with combinations of TDV_{α}^q with $\alpha_1 = 1$, $\alpha_2 = (1, \infty)$, and $\alpha_3 = (1, \infty, \infty)$ and with homogeneously fixed $\mathbf{b} = (1, 0.02)$.

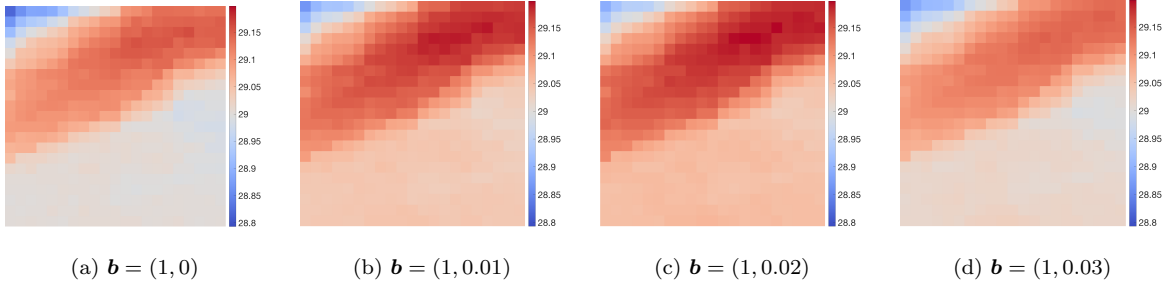


Figure 5.6: PSNR for different σ_1 (y-axis), ρ_1 (x-axis) and \mathbf{b} for Figure 5.3b with $\text{TDV}_{\alpha_1}^1 + \text{TDV}_{\alpha_3}^3$, $\alpha_1 = (1)$, $\alpha_3 = (1, \infty, \infty)$ and $\eta = 3.5$. Here $k = 2$ for Alg. 5.1, with $(\sigma_2, \rho_2) = (1, 1)$.

approach seems reasonable outside the rainbow while an anisotropic approach inside. This resulted in varying the β parameter following equations (5.4)-(5.5): in Figure 5.7d the black pixels correspond to $\beta \approx 0$ and the white pixels to $\beta \approx 1$. Indeed for $\beta \approx 0$ we expect to denoise the image following the anisotropy induced by \mathbf{v} , while for $\beta \approx 1$ we expect to denoise the image isotropically in both \mathbf{v} and \mathbf{v}_{\perp} directions. In order to compute the vector field \mathbf{v} as in Figure 5.7e, we did not apply the regularisation step (5.2) and we did not iterate Algorithm 5.1 since both the resulting \mathbf{v} and \mathbf{b} seem good enough for our purposes, performing better than BM3D in Figure 5.7c, with less wavy artefacts and a smoother global structure.

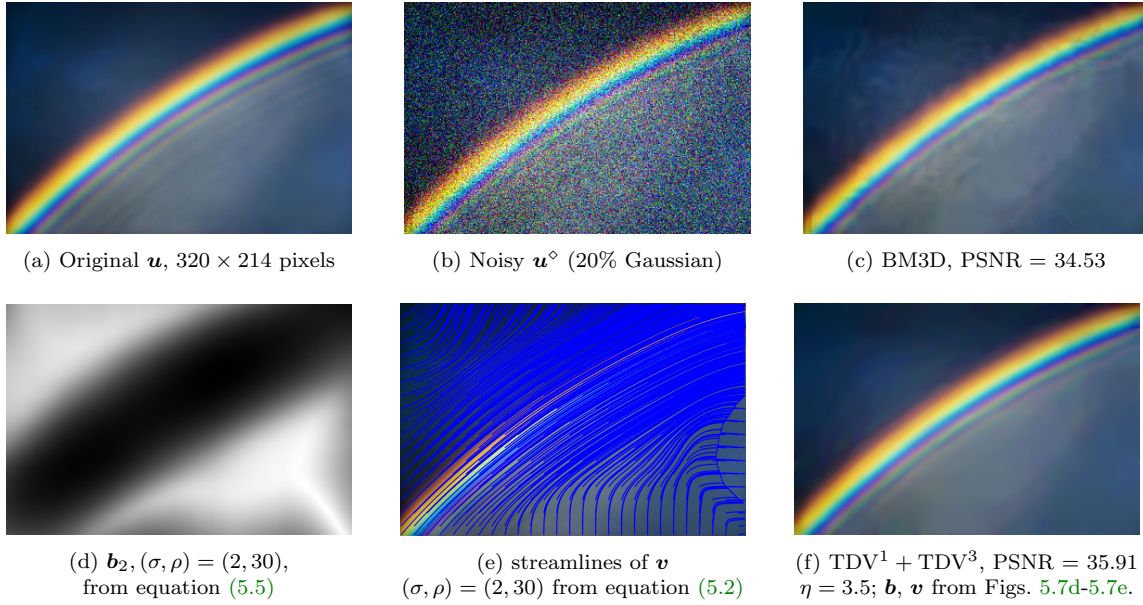


Figure 5.7: Denoising of RGB rainbow (photo by M.P. Markkanen, CC-BY-SA-4.0 license).

Desert image. The desert image in Figure 5.8a is a mix of anisotropic and isotropic information. We denoised Figure 5.8b, corrupted again with 20% of Gaussian noise in each color channel, with $(\sigma, \rho) = (3, 1.5)$ and $\gamma = 0.1$ to estimate \mathbf{v} in Figure 5.8e as described before. We also allowed $\beta(\cdot)$ to vary across the domain and we did not refine \mathbf{v} with further iterations. Here, BM3D in Figure 5.8c performed slightly better than our approach due to the wrong estimation of \mathbf{v} along some dune waves: this is clearly visible in Figures 5.8d and 5.8e where both the wrong estimation of \mathbf{v} and the isotropy requirement of β result in a smoothing performance, as shown in the zooms of Figures 5.8g and 5.8h. However, we recall that BM3D is a non-local method and better performances than local methods are expected. Nevertheless, since this kind of images have patterns and structures at different scales such that they cannot be captured by a single global structure tensor, we expect that the reconstruction quality can be improved, e.g. by a structure tensor workflow with locally adapting parameters (σ, ρ) .

6. Other imaging applications with the joint model. In what follows we focus on the joint minimisation model (1.13) for the applications of image zooming and surface interpolation.

6.1. Wavelet Zooming. In this section we apply our regularisation to wavelet-based image zooming as in [10]. Here, the data fidelity term is modelled by a wavelet transformation operator. Let $\phi \in L^2(\mathbb{R})$, $\psi \in L^2(\Omega)$ be the scaling and mother wavelet function, respectively. Then, a Riesz basis of $L^2(\Omega)$ is obtained from translations and rotations of ϕ and ψ . Here, we will consider only functions ϕ with compact support, yielding a compactly supported basis elements. Let $R \in \mathbb{Z}$ be a resolution level and $M_R, (L_j)_{j \leq R}$ be finite index sets in \mathbb{Z}^2 , then:

- a Riesz basis of $L^2((0, 1) \times (0, 1))$ is $(\phi_{R, \mathbf{k}})_{\mathbf{k} \in M_R}, (\psi_{j, \mathbf{k}})_{j \leq R, \mathbf{k} \in L_j}$;
- the dual Riesz basis of the above is defined as $(\tilde{\phi}_{R, \mathbf{k}})_{\mathbf{k} \in M_R}, (\tilde{\psi}_{j, \mathbf{k}})_{j \leq R, \mathbf{k} \in L_j}$.

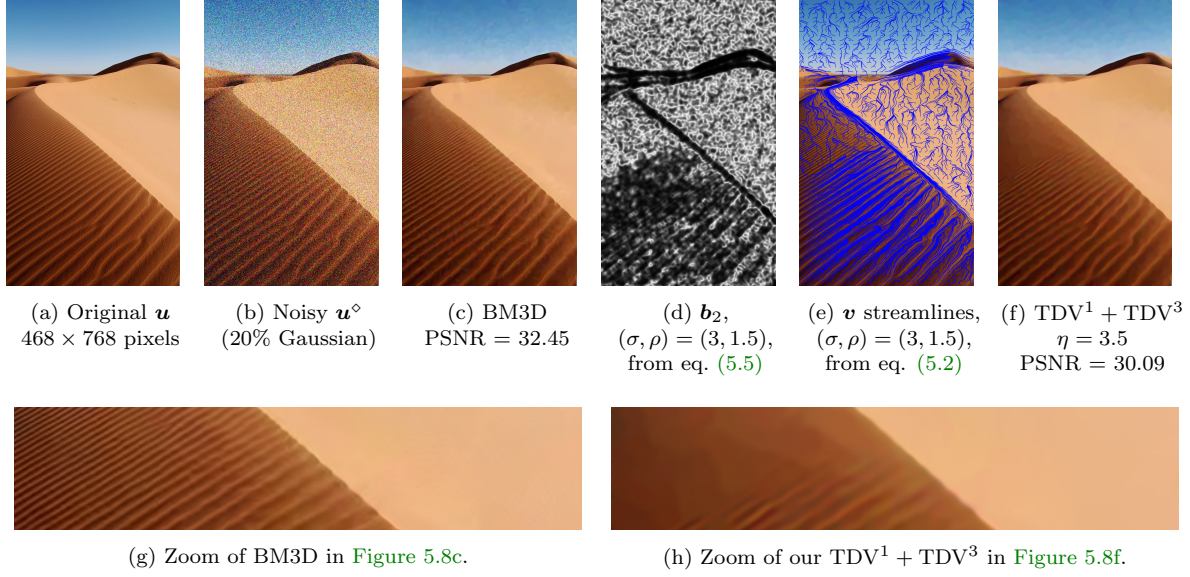


Figure 5.8: Denoising of RGB desert (photo by Rosino, CC-BY-SA-2.0 license).

Thus, the following decomposition holds:

$$u = \sum_{\mathbf{k} \in M_R} (u, \phi_{R,\mathbf{k}})_2 \tilde{\phi}_{R,\mathbf{k}} + \sum_{j \leq R, \mathbf{k} \in L_j} (u, \psi_{j,\mathbf{k}})_2 \tilde{\psi}_{j,\mathbf{k}}.$$

Let $u_0 \in \text{span} \{ \tilde{\phi}_{R,\mathbf{k}} \mid \mathbf{k} \in M_R \}$ be a low resolution version of u given by $((u_0, \phi_{R,\mathbf{k}})_2)_{\mathbf{k} \in M_R}$, where the unknown u is such that $(u, \phi_{R,\mathbf{k}})_2 = (u_0, \phi_{R,\mathbf{k}})_2$, for all $\mathbf{k} \in M_R$, and

$$u \in L^2(\Omega) = \text{span} \left(\left\{ \tilde{\phi}_{R,\mathbf{k}} \mid \mathbf{k} \in M_R \right\} \cup \left\{ \tilde{\psi}_{j,\mathbf{k}} \mid j \leq R, \mathbf{k} \in L_j \right\} \right).$$

The wavelet-based zooming problem with higher order total directional regularisers reads as

$$u^* \in \arg \min_{u \in \mathbb{R}^{|\Omega^h|}} \sum_{q=1}^Q \text{TDV}_{\alpha_q}^q(u, \mathcal{M}) + \mathcal{I}_{U_D}(u),$$

where $U_D = \{ u \in L^2(\Omega) \mid (u, \phi_{R,\mathbf{k}})_2 = (u_0, \phi_{R,\mathbf{k}})_2, \text{ for all } \mathbf{k} \in M_R \}$ and \mathcal{I}_{U_D} is the convex indicator function w.r.t. U_D , see [10] for more details. Since we did not downsample the original image, we avoided artefacts introduced by algorithms for reducing the image but at the same time no ground truth is available. Results based on CDF 9/7 wavelet are shown in Figure 6.1 (grey-scale) and in Figure 6.2 (colour).

6.2. Surface Interpolation. In this experiment, we aim to reconstruct a surface from scattered height data available in Ω . The available data lies on partially occluded isolines or on random points in Ω and the challenge is to interpolate them by preserving the anisotropic features via the reconstruction of a suitable vector field \mathbf{v} . Before presenting our approach for this problem using TDV_{α}^q , we briefly review the state-of-the-art for surface interpolation.

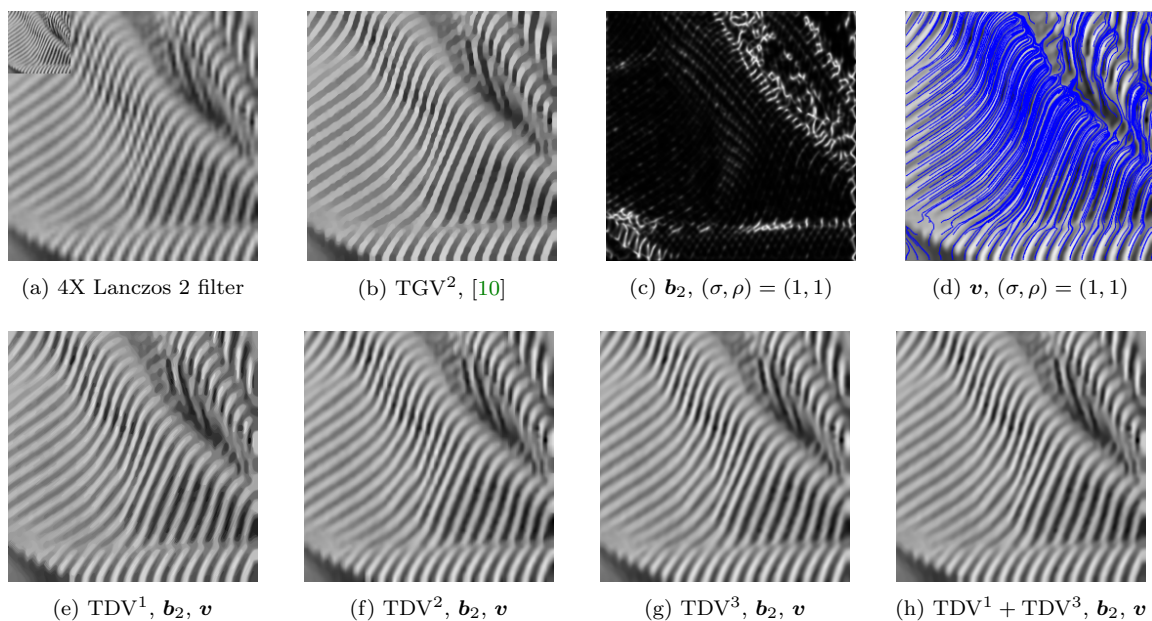


Figure 6.1: Wavelet-based zooming with CDF 9/7.

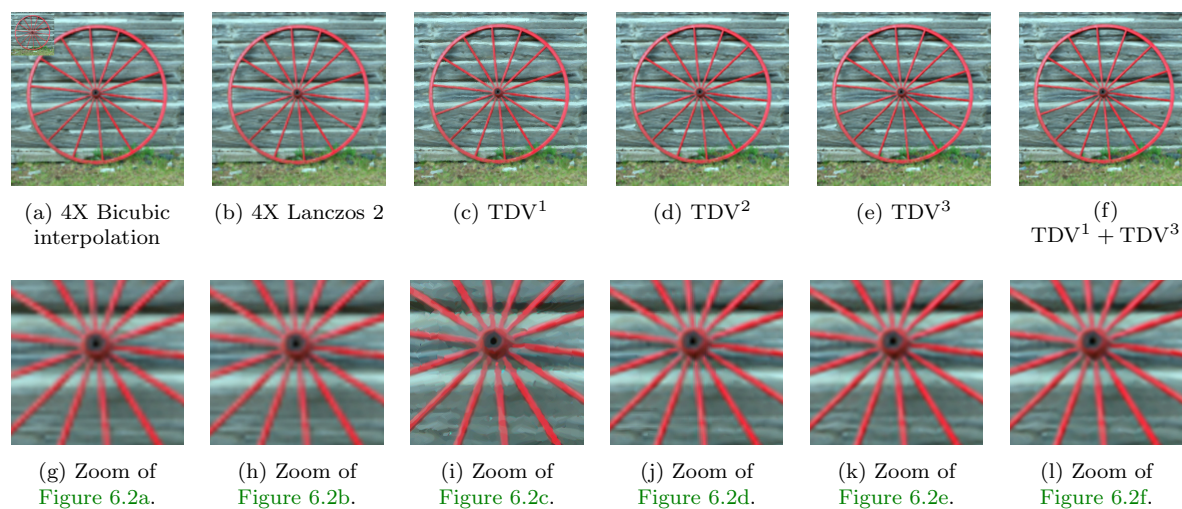


Figure 6.2: Wavelet-based zooming with CDF 9/7. Image from the MorgueFile archive.

Related works. The reconstruction of surfaces from scattered height values has been approached in two different ways in the literature: based on explicit and implicit models. Surface interpolation is sometimes also addressed as *digital elevation map* (DEM) problem.

In this paper we focus on implicit surface interpolation which has the advantage of being independent with respect to parametrization. Here the surface is an implicit function of height values over the domain. Two prominent methods in this range are the Thin Plate Spline (TPS) [36] and the *Absolute Minimizing Lipschitz Extension* (AMLE) [2] approach. TPS is a flexible

approach since it can embed both grey values and gradient information. However, it has the drawback to be a fourth order isotropic method and the resulting interpolated surface is isotropically smooth. AMLE, on the other hand, is able to interpolate data given in isolated points and on curves but it fails to interpolate slopes of a surface, resulting in C^1 , see [47].

For interpolating surfaces with sharp features, e.g. strong creases, and possibly non-smooth features, e.g. corners in a pyramid, it seems promising therefore to consider (higher-order) total variation (TV) regularisers for surface interpolation.

Our main model approach here is [34], where a third-order directional total variation regulariser has been proposed that reads for a given vector field \mathbf{v} as

$$(6.1) \quad E(u) = \int_{\Omega} \|\nabla_{\mathbf{v}}(\nabla^2 u)\|_2,$$

where $\nabla_{\mathbf{v}}^3 u = \nabla(\nabla^2 u) \cdot \mathbf{v}$ is the directional derivative of the Hessian of u , along \mathbf{v} . Note that this is a special case of TDV_{α}^Q with $Q = 3$, $a = 1$, $\mathbf{b} = (1, 0)$, $\mathbf{v} = (\cos \theta, \sin \theta)$, i.e. $\mathcal{M} = (\mathbf{I}, \mathbf{I}, \mathbf{M})$ and $\mathbf{M} = \Lambda_{\mathbf{b}}(\mathbf{R}_{\theta})^T$, leading to $\nabla_{\mathbf{v}}^3 u \equiv \mathbf{M} \nabla \otimes (\nabla^2 u)$.

The estimation of \mathbf{v} is crucial to obtain a good quality result. In [34], \mathbf{v} has been computed as a two step minimization-regularisation problem by solving firstly

$$\tilde{\mathbf{v}} = \arg \min_{\mathbf{y}: \|\mathbf{y}\|_2=1} \left\| K_{\sigma} * \nabla \left(\frac{\nabla u}{|\nabla u|} \right) (\mathbf{x}) \mathbf{y} \right\|_2$$

and then applying to $\tilde{\mathbf{v}}$ the same regularisation step in (5.2), where $w(\mathbf{x})$ is a weight chosen as the largest singular value of $K_{\sigma} * \nabla \left(\frac{\nabla u}{|\nabla u|} \right)$ and γ is a regularising parameter smoothing the vector field where u is almost planar and preserving the local values of $\tilde{\mathbf{v}}$ for level lines of large curvature. As last step, \mathbf{v} is normalised to be unitary.

Another directional interpolation model for u and \mathbf{v} appears in [8]: differently from our approach in this paper, it requires knowledge of the vector field \mathbf{v} prior to the interpolation.

In this section, we generalize the approach of [34] for the reconstruction of a surface, given scattered height values lying (possibly) on partial contour lines. Differently from Section 5, the unitary vector field \mathbf{v} is reconstructed in the missing domain as follows.

Let Ω^h be a 2D domain ($d = 2$) and $u^{\diamond, h}$ be sparse sampled height values. In the following, the projection onto the data available $u^{\diamond, h}$ is identified by the operator \mathcal{S} . We aim to find the interpolated surface $u \in \mathbb{R}^{|\Omega^h|}$, driven by the unitary directions $\mathbf{v} \in \mathbb{R}^{|\Gamma^h|}$. Let $\mathcal{M} = (\mathcal{M}_1, \dots, \mathcal{M}_Q)$ be a collection of weighting fields, where for a fixed q each collection \mathcal{M}_q is defined as $\mathcal{M}_q = (\mathbf{I}, \dots, \mathbf{I}, \mathbf{M})$ with explicit dependence on \mathbf{v} . We solve by Algorithm 6.1, alternatingly:

$$(6.2) \quad u^{\star} \in \arg \min_{u \in \mathbb{R}^{|\Omega^h|}} \sum_{q=1}^Q \text{TDV}_{\alpha_q}^q(u, \mathcal{M}_q^a(\mathbf{v})) + \frac{\eta}{2} \|\mathcal{S}u - u^{\diamond}\|_2^2,$$

$$(6.3) \quad \mathbf{v}^{\star} \in \arg \min_{\mathbf{v} \in \mathbb{R}^{|\Gamma^h|}} \mu \text{TV}(\mathbf{v}) + \zeta \int_{\Omega} \left(1 - \mathbf{v} \cdot \frac{\nabla u}{|\nabla u|} \right)^2 d\mathbf{x},$$

with the primal-dual in [Algorithm 4.2](#) for (6.2) and a classic primal-dual for (6.3). In particular, in (6.3) we identify $F(\mathbf{v}) = \text{TV}(\mathbf{v})$ for regularising the vector field \mathbf{v} and $G(\mathbf{v}) = \left\| 1 - \mathbf{v} \cdot \frac{\nabla u}{|\nabla u|} \right\|_{L^2}^2$ for normalising \mathbf{v} in the direction of the normalised gradient [4].

Algorithm 6.1 Alternating scheme for the surface interpolation problem in (6.2) and (6.3)

Input : the sparse data u^\diamond in Ω .
Parameters : $\alpha_q = (\alpha_j)_{j=0}^{q-1}$ for $q = 1, \dots, Q$ with $\alpha_0 = 1$ and $+\infty$ otherwise, $\eta > 0$, $\mu, \zeta > 0$.
Initialization : random u^0 and \mathbf{v}^0 , $\mathcal{S}(u^0) = u^\diamond$, $t = 0$.
Update : u^t and \mathbf{v}^t as follows.
while stopping criterion is not satisfied do
 $u^{t+1} \in \arg \min_{u \in \mathbb{R}^{|\Omega^{h_1}|}} \sum_{q=1}^Q \text{TDV}_{\alpha_q}^q(u, \mathcal{M}_q(\mathbf{v}^t)) + \frac{\eta}{2} \|\mathcal{S}u - u^\diamond\|^2$; // Minimization w.r.t. u
 $\mathbf{v}^{t+1} \in \arg \min_{\mathbf{v} \in \mathbb{R}^{|\Gamma^{h_1}|}} \mu \text{TV}(\mathbf{v}) + \zeta \int_{\Omega} \left(1 - \mathbf{v} \cdot \frac{\nabla u^{t+1}}{|\nabla u^{t+1}|} \right)^2 dx$; // Minimization w.r.t. \mathbf{v}
 Update $\mathcal{M}_q(\mathbf{v}^{t+1})$ for each $q = 1, \dots, Q$; // update the weights
end
return $(u^*, \mathbf{v}^*) = (u^{t+1}, \mathbf{v}^{t+1})$.

Minimization with respect to u . Fixing an unitary vector field \mathbf{v}^t , the minimization problem (6.2) is convex with respect to u and the minimization problem can be solved via primal-dual [Algorithm 4.2](#) without acceleration due to the lack of strong convexity of the projection map \mathcal{S} , which results in a non-smooth dual problem.

Minimization with respect to \mathbf{v} . Fixing u^{t+1} , the minimization problem (6.3) can be solved by the primal-dual algorithm with

$$F(\mathbf{v}) = \mu \text{TV}(\mathbf{v}) \quad \text{and} \quad G(\mathbf{v}) = \zeta \int_{\Omega} \left(1 - \mathbf{v} \cdot \frac{\nabla u^{t+1}}{|\nabla u^{t+1}|} \right)^2 dx.$$

Let $\mathbf{s} = K\mathbf{v}$, $K = \nabla$ and $K^* = -\text{div}$. Then, the proximal of F^* , with $F(\mathbf{v}) = \mu \text{TV}(\mathbf{v})$, is the projection onto the polar ball:

$$\mathbf{prox}_{\sigma F^*}(\mathbf{s}) = \frac{\mathbf{s}}{\max(1, \mu^{-1} \|\mathbf{s}\|_2)}.$$

The proximal map of G at $\hat{\mathbf{v}} = (\hat{v}_1, \hat{v}_2)$, for $\mathbf{p} = \nabla u^{t+1} / |\nabla u^{t+1}| = (p_1, p_2)$, reads as

$$\mathbf{prox}_{\tau G}(\hat{\mathbf{v}}) = \arg \min_{\mathbf{v} \in \mathbb{R}^2} \zeta \|1 - \mathbf{v} \cdot \mathbf{p}\|_2^2 + \frac{1}{2\tau} \|\mathbf{v} - \hat{\mathbf{v}}\|_2^2,$$

thus

$$\mathbf{prox}_{\tau G}(\hat{\mathbf{v}}) = \begin{pmatrix} 2\zeta p_1^2 + \tau^{-1} & 2\zeta p_1 p_2 \\ 2\zeta p_1 p_2 & 2\zeta p_2^2 + \tau^{-1} \end{pmatrix}^{-1} \begin{pmatrix} 2\zeta p_1 + \tau^{-1} \hat{v}_1 \\ 2\zeta p_2 + \tau^{-1} \hat{v}_2 \end{pmatrix}.$$

Since G is strongly-convex, we use the accelerated scheme (4.15), with K instead of \mathcal{K} .

Numerical Results. We tested [Algorithm 6.1](#) in MATLAB on synthetic and real surfaces. Differently from [\[34\]](#), we did not use CVX or MOSEK, making our approach suitable for larger surfaces, beyond the variable size limit imposed by CVX. In what follows, we will use [\(5.7\)](#) for solving [\(6.2\)](#) and we will test both single and joint directional regularisers, namely $\mathbf{a} = (0, 1, 0)$, $\mathbf{a} = (0, 0, 1)$ and $\mathbf{a} = (0, \alpha_{2,0}, \alpha_{3,0})$, with $\alpha_{2,0}$ and $\alpha_{3,0}$ to be chosen appropriately for the situation. For a better visualization of the results, a divergence RGB colormap in the range $([0.230, 0.299, 0.754], [0.706, 0.016, 0.150])$ has been applied.

Pyramid dataset from [\[34\]](#). A pyramid with height data available on three contour lines and no extra information on the tip is given, so as to test whether our model can reconstruct it. We initialize u^0 and v^0 randomly. In [Figure 6.3](#), we report in the first column the location of the available data (top) and the ground truth (bottom); in the second column the random initialization of v^0 (top) and u^0 (bottom); in the third, fourth and fifth columns we report the results from different orders of directional regularisers, namely $\mathbf{a} = (0, 1, 0)$, $\mathbf{a} = (0, 1, 0)$ and $\mathbf{a} = (0, 1, 1)$, with one level of anisotropy $a = 1$. The similarity of the resulting vector fields in [Figure 6.3](#), despite the different derivative orders involved in the minimisation with respect to u , shows the robustness of the computation of v for such problem. Visual results suggest that a combination between second and third order directional regularisers, e.g. $\mathbf{a} = (0, \alpha_{2,0}, \alpha_{3,0})$, is desirable since it smooths the second-order result without losing its features.

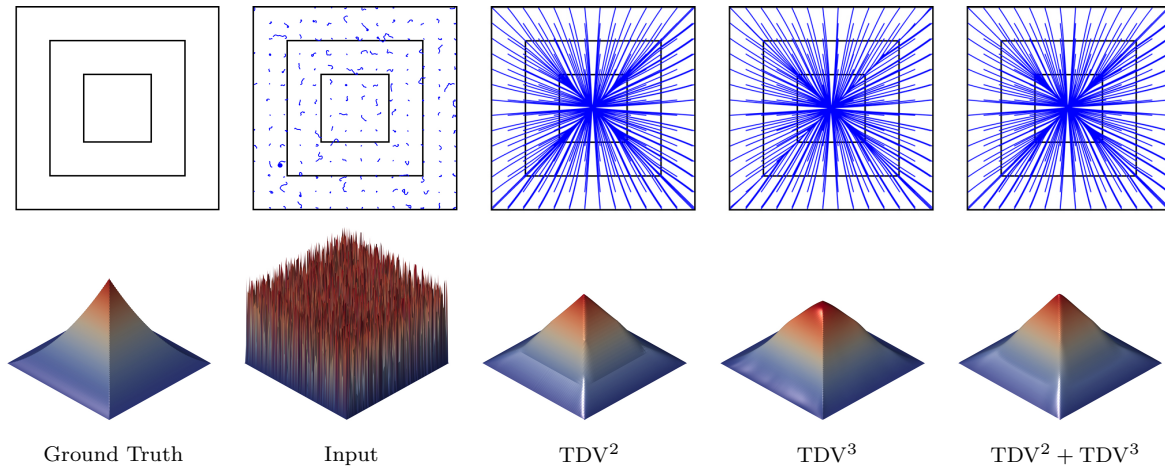


Figure 6.3: Pyramid results: 10 iterations of [Algorithm 6.1](#). Parameters: $\eta = 100$, $\mu = \zeta = 1$.

SRTM dataset from [\[54\]](#). This dataset is part of the *Shuttle Radar Topography Mission* (SRTM) [\[54\]](#) NASA mission so as to obtain elevation data for most areas of the world. We download `.hgt` “height” binary data files from [\[6\]](#), where by selection of latitude and longitude coordinates we get 1×1 degree tiles of 1-arc seconds resolution (around 30 m per pixel). We selected some famous mountains within Italy in [Figure 6.4](#): Etna volcano (Sicily), Baldo Mountain (Verona), Vesuvio volcano (Naples), Brenner border (Sterzing) and Gran Sasso (L’Aquila), with image size domain of 250×250 pixels. As input, we randomly sampled about 7% of sparse data on level lines and isolated points, to be interpolated with $0.1\text{TDV}^2 + \text{TDV}^3$.

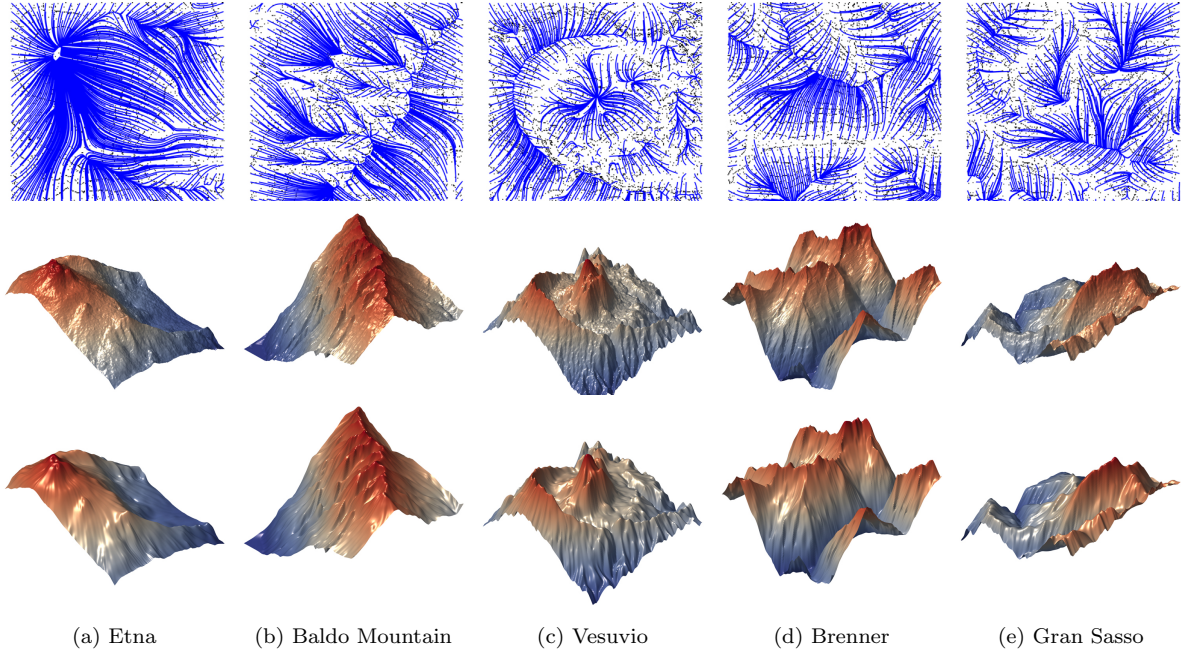


Figure 6.4: The dataset from [54]. First row: height location (black), streamlines of \mathbf{v} (blue). Second row: ground truth. Third Row: $0.1\text{TDV}^2 + \text{TDV}^3$ results, $\mu = \zeta = 1$, $\eta = 1000$.

Atomic Force Microscopy dataset from [44]. Atomic force microscopy (AFM), or scanning probe microscopy (SPM), is a topography imaging technique commonly used in the detection of cancer cells in cellular biology: it scans objects at high resolution while recording their topographical information. In [39], the study of a compressed sensing approach on AFM images was motivated by the reduction of the image acquisition time for multiple reasons, e.g. to minimize the operator time spent at the equipment [28], to allow time-dependent dynamic processes [48] and to minimize the interaction of instruments with specimens so as to reduce potential risks of damages [37]. Therefore, the authors proposed to speed up the sampling procedure by scanning height data on spirals rather than exploring pixel by pixel, so as to reconstruct the missing data via compressed sensing. The authors define the under-sampling ratio as $\rho = L/L_{ref}$, where L is the length of the spiral path followed by the probe for acquiring the data and L_{ref} is the distance travelled by the probe in pixels during the raster scan. Note that L also counts the path outside the imaging domain due to smooth movement requirement of the probe, while L_{ref} is approximated by the value $2 \cdot \#\text{pixels}$ and the factor of two is due by the usual approach to acquire two topography buffers, even if only one is used for the visualization. In order to test our reconstruction method based on the directional regularisers, we downloaded the open source AFM .mi dataset of 512×512 height values from [44], exported in ASCII text via the open-source software Gwyddion and imported in MATLAB. Our input are AFM surfaces of size 256×256 obtained by slicing the

original surface, for comparison purposes following [39]. We show the results in Figure 6.5 for the ground truth image in Figure 6.5a, with different under-sampling ratio ρ , see Figures 6.5c and 6.5d. In Figure 6.5b we compare the structural similarity index (SSIM) [56] for our results (producing the black line of scores on the top of the graph) with [39, Figure 7], where iterative hard thresholding (IHT), iterative soft thresholding (IST), their weighted version (w-IHT and w-IST) and Basis Pursuit Denoising (BPDN) were tested: we conclude that our approach is robust throughout different under-sampled data, with good quality surfaces in terms of SSIM.

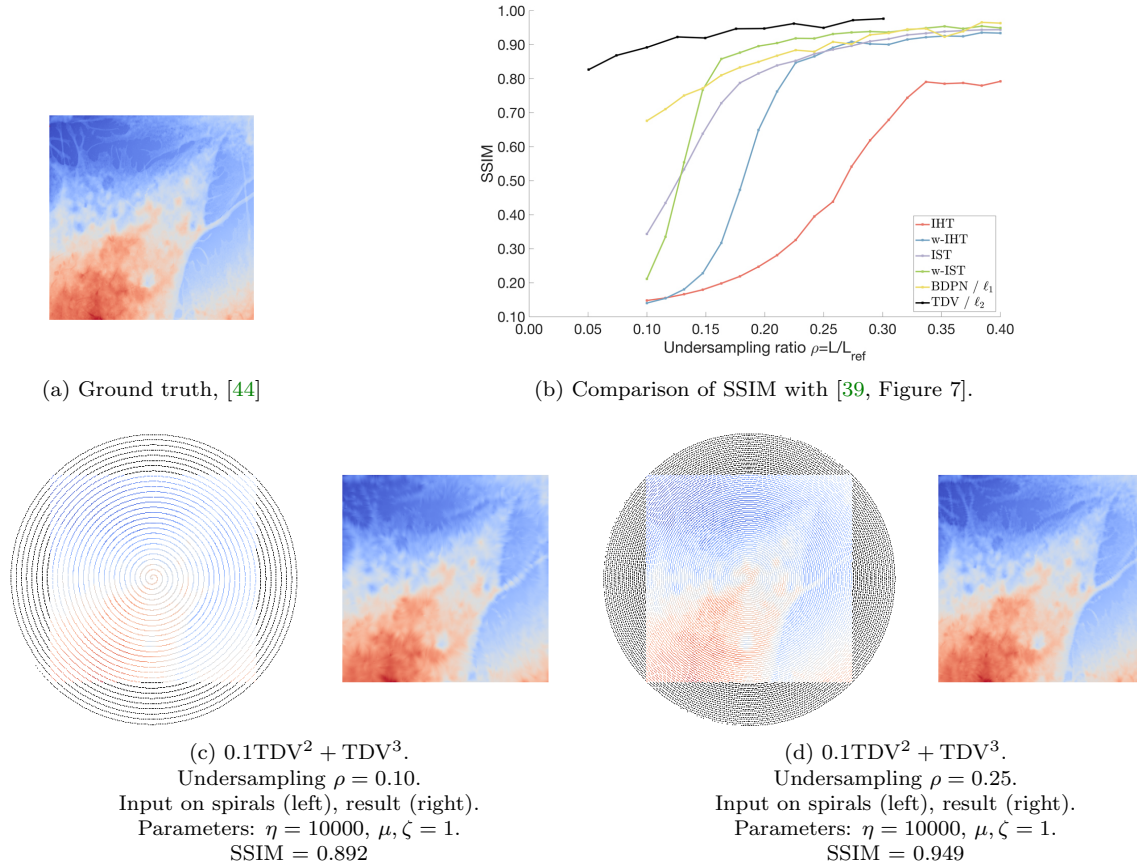


Figure 6.5: AFM reconstruction with Algorithm 6.1 from CC BY 4.0 data in [44].

7. Conclusions. In this work, we have shown that embedding anisotropic directional information into higher order derivatives improves the performance of total variation regularization in many imaging applications where anisotropy plays a crucial role. In particular, we presented results for image denoising, image zooming and interpolation of scattered measurements, with details on the numerical discretisation and the solution via a primal-dual hybrid gradient algorithm. Among the range of experiments provided, we emphasise that our ap-

proach is particularly suitable for the reconstruction task from scattered data, motivating the interest in studying the proposed energy. With this we provided a precise discrete framework which extends the works [34, 20, 11, 10], bringing higher-order total variation together with spatially-varying anisotropy. The continuous model is analysed in the companion paper [42],

Acknowledgements. The authors are grateful to Dr. Martin Holler, University of Graz (Austria) for the useful discussions and to Prof. Thomas Arildsen, Aalborg University (Denmark) for the AFM data.

REFERENCES

- [1] T. AACH, C. MOTA, I. STUKE, M. MUHLICH, AND E. BARTH, *Analysis of Superimposed Oriented Patterns*, IEEE Transactions on Image Processing, 15 (2006), pp. 3690–3700, <https://doi.org/10.1109/TIP.2006.884921>.
- [2] A. ALMANSA, F. CAO, Y. GOUSSEAU, AND B. ROUGE, *Interpolation of digital elevation models using AMLE and related methods*, IEEE Transactions on Geoscience and Remote Sensing, 40 (2002), pp. 314–325, <https://doi.org/10.1109/36.992791>.
- [3] L. ALVAREZ, F. GUICHARD, P.-L. LIONS, AND J.-M. MOREL, *Axioms and fundamental equations of image processing*, Archive for Rational Mechanics and Analysis, (1993).
- [4] C. BALLESTER, M. BERTALMIO, V. CASELLES, G. SAPIRO, AND J. VERDERA, *Filling-in by joint interpolation of vector fields and gray levels*, IEEE Transactions on Image Processing, 10 (2001), pp. 1200–1211, <https://doi.org/10.1109/83.935036>.
- [5] I. BAYRAM AND M. E. KAMASAK, *Directional total variation*, IEEE Signal Processing Letters, 19 (2012), pp. 781–784, <https://doi.org/10.1109/LSP.2012.2220349>.
- [6] F. BEAUDUCEL, *READHGT: Import/download NASA SRTM data files (.HGT)*, 2012, <https://www.mathworks.com/matlabcentral/fileexchange/36379>.
- [7] B. BERKELS, M. BURGER, M. DROSKE, O. NEMITZ, AND M. RUMPF, *Cartoon Extraction Based on Anisotropic Image Classification*, in Vision, Modeling, and Visualization Proceedings, 2006, pp. 293–300, <http://numod.ins.uni-bonn.de/research/papers/public/BeBuDr06.pdf>.
- [8] T. R. BIN WU AND X.-C. TAI, *Sparse-data based 3D surface reconstruction for cartoon and map*, Internal report, UCLA, (2017), <ftp://ftp.math.ucla.edu/pub/camreport/cam17-38.pdf>.
- [9] P. BLOMGREN AND T. F. CHAN, *Color TV: Total Variation methods for restoration of vector-valued images*, IEEE Transactions on Image Processing, 7 (1998), pp. 304–309, <https://doi.org/10.1109/83.661180>.
- [10] K. BREDIES AND M. HOLLER, *A TGV Regularized Wavelet Based Zooming Model*, Springer, 2013, pp. 149–160, https://doi.org/10.1007/978-3-642-38267-3_13.
- [11] K. BREDIES, K. KUNISCH, AND T. POCK, *Total Generalized Variation*, SIAM Journal on Imaging Sciences, 3 (2010), pp. 492–526, <https://doi.org/10.1137/090769521>.
- [12] V. CASELLES, A. CHAMBOLLE, D. CREMERS, M. NOVAGA, AND T. POCK, *An introduction to total variation for image analysis*, Theoretical Foundations and Numerical Methods for Sparse Recovery, 9 (2010), pp. 263–340, <https://doi.org/10.1515/9783110226157.263>.
- [13] V. CASELLES, A. CHAMBOLLE, AND M. NOVAGA, *The discontinuity set of solutions of the tv denoising problem and some extensions*, Multiscale Modeling & Simulation, 6 (2007), pp. 879–894, <https://doi.org/10.1137/070683003>.
- [14] V. CASELLES, B. TANG, AND G. SAPIRO, *Direction diffusion*, in Proceedings of the Seventh IEEE International Conference on Computer Vision (ICCV), vol. 02, 09 1999, p. 1245, <https://doi.org/10.1109/ICCV.1999.790423>.
- [15] A. CHAMBOLLE AND T. POCK, *A first-order primal-dual algorithm for convex problems with applications to imaging*, Journal of Mathematical Imaging and Vision, 40 (2011), pp. 120–145, <https://doi.org/10.1007/s10851-010-0251-1>.

- [16] A. CHAMBOLLE AND T. POCK, *An introduction to continuous optimization for imaging*, Acta Numerica, 25 (2016), pp. 161–319, <https://doi.org/10.1017/S096249291600009X>.
- [17] T. CHAN, S. ESEDOGLU, AND F. PARK, *A fourth order dual method for staircase reduction in texture extraction and image restoration problems*, in 2010 IEEE International Conference on Image Processing, 2010, pp. 4137–4140, <https://doi.org/10.1109/ICIP.2010.5653199>.
- [18] T. CHAN, A. MARQUINA, AND P. MULET, *High-order total variation-based image restoration*, SIAM Journal on Scientific Computing, 22 (2000), pp. 503–516, <https://doi.org/10.1137/S1064827598344169>.
- [19] K. DABOV, A. FOI, V. KATKOVNIK, AND K. EGIAZARIAN, *Image denoising by sparse 3-D transform-domain collaborative filtering*, IEEE Transactions on Image Processing, 16 (2007), pp. 2080–2095, <https://doi.org/10.1109/TIP.2007.901238>.
- [20] R. DALGAS KONGSKOV, Y. DONG, AND K. KNUDSEN, *Directional Total Generalized Variation Regularization*, ArXiv e-prints, (2017), <https://arxiv.org/abs/1701.02675>.
- [21] J. C. DE LOS REYES, C.-B. SCHÖNLIEB, AND T. VALKONEN, *Bilevel parameter learning for higher-order total variation regularisation models*, Journal of Mathematical Imaging and Vision, 57 (2017), pp. 1–25, <https://doi.org/10.1007/s10851-016-0662-8>.
- [22] Y. DONG AND M. HINTERMÜLLER, *Multi-scale Total Variation with Automated Regularization Parameter Selection for Color Image Restoration*, Springer, 2009, pp. 271–281, https://doi.org/10.1007/978-3-642-02256-2_23.
- [23] M. J. EHRHARDT AND M. M. BETCKE, *Multicontrast MRI reconstruction with structure-guided Total Variation*, SIAM Journal on Imaging Sciences, 9 (2016), pp. 1084–1106, <https://doi.org/10.1137/15M1047325>.
- [24] V. ESTELLERS, S. SOATTO, AND X. BRESSON, *Adaptive Regularization With the Structure Tensor*, IEEE Transactions on Image Processing, 24 (2015), pp. 1777–1790, <https://doi.org/10.1109/TIP.2015.2409562>.
- [25] J. FEHRENBACH AND J.-M. MIREBEAU, *Sparse non-negative stencils for anisotropic diffusion*, Journal of Mathematical Imaging and Vision, 49 (2014), pp. 123–147, <https://doi.org/10.1007/s10851-013-0446-3>.
- [26] W. FÖRSTNER, *A feature based correspondence algorithm for image matching*, Int. Arch. of Photogrammetry and Remote Sensing, 26 (1986), pp. 150–166.
- [27] M. GRASMAIR AND F. LENZEN, *Anisotropic total variation filtering*, Applied Mathematics and Optimization, 62 (2010), pp. 323–339, <https://doi.org/10.1007/s00245-010-9105-x>.
- [28] P. K. HANSMA, G. SCHITTER, G. E. FANTNER, AND C. PRATER, *High-Speed Atomic Force Microscopy*, Science, 314 (2006), pp. 601–602, <https://doi.org/10.1126/science.1133497>.
- [29] C. HARRIS AND M. STEPHENS, *A combined corner and edge detector*, in Proceedings of the Alvey Vision Conference, Alvey Vision Club, 1988, pp. 23.1–23.6, <https://doi.org/10.5244/C.2.23>.
- [30] M. KASS AND A. WITKIN, *Analyzing oriented patterns*, Computer Vision, Graphics, and Image Processing, 37 (1987), pp. 362–385, [https://doi.org/10.1016/0734-189X\(87\)90043-0](https://doi.org/10.1016/0734-189X(87)90043-0).
- [31] R. KIMMEL, R. MALLADI, AND N. SOCHEN, *Images as embedded maps and minimal surfaces: Movies, color, texture, and volumetric medical images*, International Journal of Computer Vision, 39 (2000), pp. 111–129, <https://doi.org/10.1023/A:1008171026419>.
- [32] F. KNOLL, K. BREDIES, T. POCK, AND R. STOLLBERGER, *Second order total generalized variation (TGV) for MRI*, Magnetic Resonance in Medicine, 65 (2011), pp. 480–491, <https://doi.org/10.1002/mrm.22595>.
- [33] S. LEFKIMMIATIS, A. ROUSSOS, P. MARAGOS, AND M. UNSER, *Structure Tensor Total Variation*, SIAM Journal on Imaging Sciences, 8 (2015), pp. 1090–1122, <https://doi.org/10.1137/14098154X>.
- [34] J. LELLMANN, J.-M. MOREL, AND C.-B. SCHÖNLIEB, *Anisotropic Third-Order Regularization for Sparse Digital Elevation Models*, in Scale Space and Variational Methods in Computer Vision, Springer, 2013, pp. 161–173, https://doi.org/10.1007/978-3-642-38267-3_14.
- [35] F. LENZEN, F. BECKER, J. LELLMANN, S. PETRA, AND C. SCHNÖRR, *A class of quasi-variational inequalities for adaptive image denoising and decomposition*, Computational Optimization and Applications, 54 (2013), pp. 371–398, <https://doi.org/10.1007/s10589-012-9456-0>.
- [36] J. MEINGUET, *Surface Spline Interpolation: Basic Theory and Computational Aspects*, Springer, 1984, pp. 127–142, https://doi.org/10.1007/978-94-009-6466-2_6.

- [37] D. MÜLLER AND Y. DUFRÊNE, *Atomic Force Microscopy: a nanoscopic window on the cell surface*, Trends in Cell Biology, 21 (2011), pp. 461 – 469, <https://doi.org/10.1016/j.tcb.2011.04.008>.
- [38] M. NIKOLOVA, *Local strong homogeneity of a regularized estimator*, SIAM Journal on Applied Mathematics, 61 (2000), pp. 633–658, <https://doi.org/10.1137/S0036139997327794>.
- [39] C. S. OXVIG, T. ARILDSEN, AND T. LARSEN, *Structure assisted compressed sensing reconstruction of undersampled AFM images*, Ultramicroscopy, 172 (2017), pp. 1–9, <https://doi.org/10.1016/j.ultramic.2016.09.011>.
- [40] K. PAPAITSOROS AND C. SCHÖNLIEB, *A combined first and second order variational approach for image reconstruction*, Journal of Mathematical Imaging and Vision, 48 (2014), pp. 308–338, <https://doi.org/10.1007/s10851-013-0445-4>.
- [41] S. PARISOTTO, *Anisotropic Variational Models and PDEs for Inverse Imaging Problems*, PhD thesis, University of Cambridge Repository, 2019, <https://doi.org/10.17863/cam.38240>.
- [42] S. PARISOTTO, S. MASNOU, AND C.-B. SCHÖNLIEB, *Higher-order total directional variation: Analysis*, SIAM Journal on Imaging Sciences, 13 (2020), pp. 474–496, <https://doi.org/10.1137/19M1239210>.
- [43] S. PARISOTTO AND C.-B. SCHÖNLIEB, *Total Directional Variation for Video Denoising*, in Scale Space and Variational Methods in Computer Vision, J. Lellmann, M. Burger, and J. Modersitzki, eds., Cham, 2019, Springer International Publishing, pp. 522–534, https://doi.org/10.1007/978-3-030-22368-7_41.
- [44] C. RANKL, *Atomic Force Microscopy Images of Cell Specimens*, 2015, <https://doi.org/10.5281/zenodo.17573>.
- [45] L. RUDIN, S. OSHER, AND E. FATEMI, *Nonlinear total variation based noise removal algorithms*, Physica D: Nonlinear Phenomena, 60 (1992), pp. 259 – 268, [https://doi.org/10.1016/0167-2789\(92\)90242-F](https://doi.org/10.1016/0167-2789(92)90242-F).
- [46] G. SAPIRO AND D. L. RINGACH, *Anisotropic diffusion of multivalued images with applications to color filtering*, IEEE Transactions on Image Processing, 5 (1996), pp. 1582–1586, <https://doi.org/10.1109/83.541429>.
- [47] O. SAVIN, *$C1$ regularity for infinity harmonic functions in two dimensions*, Archive for Rational Mechanics and Analysis, 176 (2005), pp. 351–361, <https://doi.org/10.1007/s00205-005-0355-8>.
- [48] G. SCHITTER AND M. ROST, *Scanning probe microscopy at video-rate*, Materials Today, 11 (2008), pp. 40–48, [https://doi.org/10.1016/S1369-7021\(09\)70006-9](https://doi.org/10.1016/S1369-7021(09)70006-9).
- [49] S. SETZER AND G. STEIDL, *Variational methods with higher-order derivatives in image processing*, Approximation XII, (2008), pp. 360–386.
- [50] S. SETZER, G. STEIDL, AND T. TEUBER, *Infimal convolution regularizations with discrete $l1$ -type functionals*, Communications in Mathematical Sciences, 9 (2011), pp. 797–827, <https://doi.org/10.4310/CMS.2011.v9.n3.a7>.
- [51] G. STEIDL AND T. TEUBER, *Anisotropic smoothing using double orientations*, in Scale Space and Variational Methods in Computer Vision, X.-C. Tai, K. Mørken, M. Lysaker, and K.-A. Lie, eds., Berlin, Heidelberg, 2009, Springer Berlin Heidelberg, pp. 477–489, https://doi.org/10.1007/978-3-642-02256-2_40.
- [52] U. TROTTEMBERG, C. OOSTERLEE, AND A. SCHULLER, *Multigrid*, Elsevier Science.
- [53] D. TSCHUMPERLÉ AND R. DERICHE, *Vector-valued image regularization with PDEs: a common framework for different applications*, IEEE Transactions on Pattern Analysis and Machine Intelligence, 27 (2005), pp. 506–517, <https://doi.org/10.1109/TPAMI.2005.87>.
- [54] USGS, *Shuttle Radar Topography Mission*, 2006, <https://www2.jpl.nasa.gov/srtm/>.
- [55] T. VALKONEN AND T. POCK, *Acceleration of the PDHGM on Partially Strongly Convex Functions*, Journal of Mathematical Imaging and Vision, 59 (2017), pp. 394–414, <https://doi.org/10.1007/s10851-016-0692-2>.
- [56] Z. WANG, A. C. BOVIK, H. R. SHEIKH, AND E. P. SIMONCELLI, *Image quality assessment: from error visibility to structural similarity*, IEEE Transactions on Image Processing, 13 (2004), pp. 600–612, <https://doi.org/10.1109/TIP.2003.819861>.
- [57] J. WEICKERT, *Anisotropic diffusion in image processing*, 1998.
- [58] J. WEICKERT, *Coherence-enhancing diffusion filtering*, International Journal of Computer Vision, 31 (1999), pp. 111–127, <https://doi.org/10.1023/A:1008009714131>.

- [59] J. WEICKERT AND H. SCHARR, *A scheme for coherence-enhancing diffusion filtering with optimized rotation invariance*, Journal of Visual Communication and Image Representation, 13 (2002), pp. 103–118, <https://doi.org/10.1006/jvci.2001.0495>.
- [60] C. WU AND X.-C. TAI, *Augmented Lagrangian Method, Dual Methods, and Split Bregman Iteration for ROF, Vectorial TV, and High Order Models*, SIAM Journal on Imaging Sciences, 3 (2010), pp. 300–339, <https://doi.org/10.1137/090767558>.
- [61] S. D. ZENZO, *A note on the gradient of a multi-image*, Computer Vision, Graphics, and Image Processing, 33 (1986), pp. 116 – 125, [https://doi.org/10.1016/0734-189X\(86\)90223-9](https://doi.org/10.1016/0734-189X(86)90223-9).
- [62] H. ZHANG AND Y. WANG, *Edge adaptive directional total variation*, The Journal of Engineering, (2013), <https://doi.org/10.1049/joe.2013.0116>.